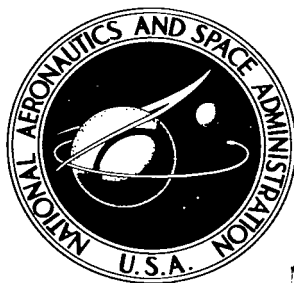


NASA TECHNICAL NOTE



NASA TN D-4185

2.1

NASA TN D-4185

LOAN COPY: RETURN
AFWL (WLJL-2)
KIRTLAND AFB, N.M.

0130856



TECH LIBRARY KAFB, NM

ENTRY FLIGHT AERODYNAMICS FROM APOLLO MISSION AS-202

by Ernest R. Hillje

Manned Spacecraft Center

Houston, Texas



0130856

NASA TN D-4185

ENTRY FLIGHT AERODYNAMICS FROM
APOLLO MISSION AS-202

By Ernest R. Hillje

Manned Spacecraft Center
Houston, Texas

NATIONAL AERONAUTICS AND SPACE ADMINISTRATION

For sale by the Clearinghouse for Federal Scientific and Technical Information
Springfield, Virginia 22151 - CFSTI price \$3.00

ABSTRACT

Inertial-platform accelerations and attitudes were used with trajectory data to calculate the flight aerodynamic characteristics of the entry configuration (command module). The flight results, in the form of aerodynamic angles, force coefficients, and coefficient ratios, were compared with trimmed wind-tunnel data predictions and with wind-tunnel data adjusted to the flight angle of attack. The comparisons showed the flight trim angle of attack to be higher than predicted at the initial high-Mach-number, low-Reynolds-number entry conditions, resulting in a correspondingly low (18 percent) lift-to-drag ratio. Both flight angle of attack and lift-to-drag ratio were essentially linear down to the high-supersonic-Mach-number region where there was good agreement with the predicted values. The areas of poor agreement were caused by poor trim-angle predictions and not by poor wind-tunnel resultant force data.

CONTENTS

| Section | Page |
|---|------|
| SUMMARY | 1 |
| INTRODUCTION | 1 |
| SYMBOLS | 2 |
| METHOD OF FLIGHT-DATA REDUCTION | 5 |
| Aerodynamic-Angle Program | 5 |
| Aerodynamic-Coefficient Program | 5 |
| ENTRY TRAJECTORY | 6 |
| PRESENTATION OF RESULTS | 6 |
| Wind-Tunnel Data | 6 |
| Wind-Tunnel Data Adjusted to Flight Angle of Attack (Hybrid Data) | 7 |
| Factors Influencing the Aerodynamic Data | 7 |
| RESULTS AND DISCUSSION | 9 |
| Aerodynamic Angles | 9 |
| Aerodynamic-Coefficient Ratios | 9 |
| Aerodynamic Body Axis Force Coefficients | 10 |
| Aerodynamic Ground-Relative Force Coefficients | 11 |
| Flight-Data Uncertainties | 12 |
| CONCLUDING REMARKS | 13 |
| REFERENCES | 14 |

TABLES

| Table | Page |
|---|------|
| I SOURCES OF AERODYNAMIC DATA PRESENTED | 15 |
| II MOVEMENT OF SPACECRAFT CENTER OF GRAVITY BASED ON REACTION-CONTROL SUBSYSTEM FUEL USAGE | 16 |

FIGURES

| Figure | Page |
|--|------|
| 1 Apollo command module CM 011 entry configuration | |
| (a) Photo of spacecraft aboard recovery ship USS Hornet looking into body +Y-axis | 17 |
| (b) Photo of spacecraft aboard recovery ship USS Hornet looking into body -Y-axis to -Z-axis | 18 |
| (c) Command module CM 011 dimensions, full-scale linear dimensions, in. | 19 |
| (d) Command module CM 011 aft heat-shield ablator | 20 |
| 2 Definition of axis systems | |
| (a) Body axis system showing positive directions of aerody- namic angles and aerodynamic body force coefficients | 21 |
| (b) Geodetic and airstream axis systems showing positive directions of aerodynamic coefficients, axes, and angles relative to the ground | 22 |
| 3 Angle-of-attack program flow diagram | 23 |
| 4 Aerodynamic-coefficient program flow diagram | 24 |
| 5 Time histories of trajectory parameters for reentry phase, Mission AS-202 | |
| (a) Altitude h , longitude Θ_{GD} , and geodetic latitude Φ_{GD} | 25 |
| (b) Airstream relative velocity V_A , flight-path angle γ_A , and azimuth σ_A | 26 |
| (c) Deceleration load factor L_f | 27 |
| (d) Dynamic pressure q_∞ | 28 |
| (e) Mach number M | 29 |
| (f) Reynolds number $Re_{\infty, d}$ based on $d = 12.833$ feet | 30 |

| Figure | Page | |
|--------|--|----|
| 6 | Extrapolated postflight reentry atmospheric data, Mission AS-202 | 31 |
| 7 | Time histories of flight aerodynamic angles | |
| | (a) Angle of attack α | 32 |
| | (b) Angle of sideslip β | 33 |
| | (c) Aerodynamic roll angle Φ_A | 34 |
| | (d) Total angle of attack α_R | 35 |
| 8 | Total flight angle of attack α_R plotted against Mach number M . Data in the low dynamic-pressure region are omitted | 36 |
| 9 | Time histories of flight aerodynamic-coefficient ratios | |
| | (a) Lift-to-drag ratio relative to ground $(L/D)_G$ | 37 |
| | (b) Side-force-to-drag ratio relative to ground $(Y/D)_G$ | 38 |
| | (c) Total lift-to-drag ratio $(L/D)_{RG}$ | 39 |
| 10 | Total flight lift-to-drag ratio $(L/D)_{RG}$ plotted against Mach number M . Data in the low deceleration-level region are omitted | 40 |
| 11 | Time histories of flight body axis coefficients | |
| | (a) Axial-force coefficient C_A | 41 |
| | (b) Resultant normal-force coefficient $C_{N,R}$ | 42 |
| | (c) Side-force coefficient C_Y | 43 |
| | (d) Normal-force coefficient C_N | 44 |
| 12 | Time histories of flight force coefficients relative to the ground | |
| | (a) Lift coefficient relative to the ground $C_{L,G}$ | 45 |
| | (b) Side-force coefficient relative to the ground $C_{Y,G}$ | 46 |
| | (c) Drag coefficient $C_{D,G}$ | 47 |
| | (d) Resultant lift coefficient $C_{L, RG}$ | 48 |
| 13 | Example of the source of the wind-tunnel data adjusted to flight angle of attack or the hybrid data method. Shown are wind- tunnel data for lift-to-drag ratio L/D plotted against angle of attack α for $M = 6.0$ | 49 |

| Figure | | Page |
|--------|--|------|
| 14 | Effects of flight-data uncertainties on the calculated aerodynamic data | |
| | (a) Total angle-of-attack α_R delta values | 50 |
| | (b) Total angle-of-attack α_R rss delta values | 51 |
| | (c) Coefficient-ratio delta values | 52 |
| | (d) Body axis coefficient delta values | 53 |
| | (e) Percent uncertainty in all flight coefficient data caused by an uncertainty of measured stagnation pressure of 3 percent of full-scale reading | 54 |

ENTRY FLIGHT AERODYNAMICS FROM

APOLLO MISSION AS-202

By Ernest R. Hillje
Manned Spacecraft Center

SUMMARY

Apollo Mission AS-202 generated the first good, continuous set of flight-measured data required to calculate the Apollo entry-configuration aerodynamic characteristics. Inertial-platform accelerations and attitude angles were used in conjunction with a best-estimated trajectory, obtained from the onboard guidance and navigation system and from radar data, to calculate flight aerodynamic angles, force-coefficient ratios, body axis force coefficients and ground-relative force coefficients. These were compared with both trim wind-tunnel data and wind-tunnel data adjusted to flight angle of attack.

The flight data showed the trim angle of attack to be higher than that predicted at the initial entry condition (near a Mach number of 28.0) which resulted in an 18-percent-lower total lift-to-drag ratio. Both the total angle of attack and the total lift-to-drag ratio were essentially linear down to a Mach number of approximately 6.0, where agreement with predicted values became very good. In addition, from a Mach number of approximately 23 down to a Mach number of approximately 1.35 the flight total lift-to-drag ratio was within the stated preflight uncertainty.

The good agreement between the flight total lift-to-drag ratio and the wind-tunnel data adjusted to flight angle of attack for the entire flight indicates that the predicted trim angle was the cause of the differences in the total lift-to-drag ratio. For this reason, and because they are not subject to the flight calculated dynamic pressure, the coefficients based on the wind-tunnel data taken at the flight angle of attack are considered to represent the best time history of the coefficient data.

INTRODUCTION

Before a flight program for a new aerodynamic configuration is established, extensive testing is usually performed throughout the expected flight flow regime. The Apollo wind-tunnel testing program, whose historical development is reported in reference 1, was initiated in early 1962 and consisted of many tests in various facilities.

To form a consistent set of preflight data for the Apollo command module (CM), which represented the entry configuration, the results of the testing program (refs. 2 to 5) were analyzed and faired with both Mach number and angle of attack. The data were then extrapolated up to the highest flight Mach numbers, where experimental data

were not available. Also, the aerodynamic characteristics were modified to account for configuration differences, such as differences in center of gravity and protuberances and asymmetry caused by the ablative material applied to the heat shield, in the tested models.

The Apollo space-flight test program began with two unmanned suborbital flights from Cape Kennedy, Florida, using uprated Saturn I launch vehicles. The first Apollo Mission (AS-201) occurred February 26, 1966, with a production CM 009 as the entry vehicle. An inertial measurement unit (IMU) was not required on this relatively simple mission, thereby precluding a detailed determination of the aerodynamic characteristics of the entry vehicle.

The second flight test, Apollo Mission AS-202, occurred August 25, 1966, with CM 011 as the entry configuration (fig. 1). Flight data in the form of inertial-platform attitudes and accelerations, and a trajectory that was reconstructed from a combination of guidance and navigation and radar-tracking data (ref. 6), were used to calculate the entry flight aerodynamic characteristics for this Apollo mission. Subsequent to the conclusion of the analysis reported in this paper, a more refined trajectory became available. The more refined trajectory was the result of further error analysis of the guidance-and-navigation data (ref. 7). Differences in the trajectory parameters began to appear near $t + 5000$ seconds. However, it was determined that these differences had no effect on the conclusions presented in this report. A unique source of the dynamic-pressure time history was the onboard surface-pressure measurements, which were incorporated into the flight aerodynamic-coefficient calculations.

The purpose of this report is to present the flight results and to compare them with the existing preflight, or ground-facility, data. From the comparison and analysis, a hybrid set of aerodynamic data is formed using a combination of flight attitudes with wind-tunnel force data. These hybrid data are considered to be the best representation of the aerodynamic coefficients. An analysis of several sources of uncertainty is also included.

SYMBOLS

| | |
|-----------------------------|--|
| A_x, A_y, A_z | acceleration along body axes, ft/sec^2 |
| $A_{x,p}, A_{y,p}, A_{z,p}$ | acceleration from X-, Y-, and Z-axes of inertial platform, ft/sec^2 |
| C_A | aerodynamic body axis axial-force coefficient, $\frac{-m A_x}{q_\infty S}$ |
| $C_{D,G}$ | aerodynamic drag coefficient relative to the ground and along V_A |
| $C_{L,G}$ | aerodynamic lift coefficient relative to the ground, perpendicular to V_A , and in the orbital plane |

| | |
|------------------|--|
| $C_{L, RG}$ | resultant, or total, aerodynamic lift coefficient, $\sqrt{C_{L, G}^2 + C_{Y, G}^2}$ |
| C_N | aerodynamic body axis normal-force coefficient, $\frac{-mA_z}{q_\infty S}$ |
| $C_{N, R}$ | aerodynamic body axis resultant, or total, normal-force coefficient, $\sqrt{C_Y^2 + C_N^2}$ |
| C_Y | aerodynamic body axis side-force coefficient, $\frac{+mA_y}{q_\infty S}$ |
| $C_{Y, G}$ | aerodynamic side-force coefficient relative to the ground and perpendicular to the orbital plane |
| d | spacecraft reference diameter, 12.833 ft |
| g | acceleration of gravity at the surface of the earth, 32.1740 ft/sec ² |
| h | spacecraft altitude, ft |
| L_f | deceleration load factor, $\frac{\sqrt{A_x^2 + A_y^2 + A_z^2}}{g}$, g |
| L/D | lift-to-drag ratio |
| $(L/D)_G$ | lift-to-drag ratio relative to the ground |
| $(L/D)_{RG}$ | resultant, or total, lift-to-drag ratio, $\frac{\sqrt{C_{L, G}^2 + C_{Y, G}^2}}{C_{D, G}}$ |
| M | Mach number |
| m | spacecraft mass, slugs |
| q_∞ | dynamic pressure, lb/ft ² |
| $Re_{\infty, d}$ | Reynolds number based on d = 12.833 ft |
| S | reference area, ft ² |
| T_{GD2A} | transformation matrix, geodetic to airstream axes |

| | |
|--------------------------|---|
| T_{GD2I} | transformation matrix, geodetic to earth-centered inertial axes |
| T_{I2P} | transformation matrix, earth-centered inertial to inertial-platform axes |
| T_{P2B} | transformation matrix, inertial-platform to spacecraft body axes |
| t | elapsed time from time of range zero, which is the first integral second of range time prior to the instant of Saturn instrument-unit umbilical disconnect, sec |
| u, v, w | individual components of spacecraft velocity with respect to the airstream along the body X-, Y- and Z-axes, ft/sec |
| u_{GD}, v_{GD}, w_{GD} | individual components of spacecraft velocity with respect to the airstream along the X_{GD} -, Y_{GD} -, and Z_{GD} -axes, ft/sec |
| V_A | total spacecraft velocity with respect to airstream, ft/sec |
| X, Y, Z | body axis system |
| X_A, Y_A, Z_A | airstream axis system |
| X_{GD}, Y_{GD}, Z_{GD} | geodetic axis system |
| $(Y/D)_G$ | side-force-to-drag ratio relative to the ground |
| α | angle of attack, deg |
| α_R | resultant, or total, angle of attack, deg |
| β | angle of sideslip, deg |
| γ_A | flight-path angle of V_A , deg |
| Δ | a difference from the nominal value of a quantity, or delta value |
| Θ, Φ, Ψ | inertial-platform gimbal angles in pitch, roll, and yaw, deg |
| Θ_{GD} | longitude of the spacecraft, deg |
| σ_A | azimuth of V_A , deg |

| | |
|-------------|--|
| Φ_A | aerodynamic roll angle, deg |
| Φ_{GD} | geodetic latitude of the spacecraft, deg |

METHOD OF FLIGHT-DATA REDUCTION

Two separate, but related, computation programs were used to obtain the flight aerodynamic characteristics from onboard measurements and from the best estimate of trajectory (BET). The first program calculated the aerodynamic angles, and the second calculated the individual coefficients and coefficient ratios. Figure 2(a) shows the relationship of the aerodynamic angles and coefficients to the body axis systems, and figure 2(b) shows the coefficients and coefficient ratios relative to the ground.

Aerodynamic-Angle Program

This program is essentially a series of three matrix transformations performed to obtain the components of the velocity of the spacecraft relative to the air in the body axis system (fig. 3). The elements of the first transformation matrix T_{I2P} are constant and relate the earth-centered inertial frame (which is referenced to Greenwich mean time, as of midnight the day before launch) to the Apollo IMU (or platform frame) where guidance reference release occurred at $t + 1.33$ seconds.

These matrix elements are calculated from the geodetic position of the inertial platform and from the aiming azimuth at platform release. The elements of the second matrix T_{P2B} relate the inertial-platform frame to the body axis system of the spacecraft through the IMU gimbal angles. The third matrix T_{GD2I} relates the geodetic frame to the earth-centered inertial frame when the geodetic position of the spacecraft and the elapsed time from lift-off are known. The spacecraft velocity relative to the airstream in the geodetic frame is resolved into the body frame using the three preceding matrix transformations. Then the aerodynamic angles can be calculated.

Aerodynamic-Coefficient Program

This program uses inertial-platform accelerometer measurements to calculate the force coefficients. As shown in figure 4, these accelerations are transformed into the body axis system and then corrected for any rotational accelerations (due to the distance between the IMU and the spacecraft center of gravity (c. g.)) before being put into coefficient form. The flight aerodynamic-body force coefficients are calculated using these translational accelerations and the calculated dynamic pressure. The coefficients are then transformed into a rectangular coordinate frame relative to the ground. This frame is shown in figure 2(b) and is defined by the plane formed by the airstream velocity vector V_A and the geodetic Z-axis Z_{GD} , which is also in the orbital plane. The aerodynamic parameters relative to the orbital plane are those used to shape the trajectory. In-plane parameters control longitudinal (down) range, and

parameters perpendicular to this plane control lateral (cross) range. Although the drag coefficient $C_{D,G}$ is in the ground-relative frame, it is identical to the conventional drag coefficient, that is, the coefficient along the free-stream velocity vector. The resultant lift coefficient $C_{L,RG}$ is the total force coefficient perpendicular to the free-stream velocity vector. Coefficient ratios relative to the ground (and to the orbital plane) as well as resultant, or total, lift-to-drag ratio are also calculated as shown in figure 2(b).

ENTRY TRAJECTORY

Several trajectory parameters that are related to entry aerodynamics are included for completeness. For purposes of this report, the entry trajectory begins at an altitude of 400 000 feet and ends at drogue-parachute deployment time (at approximately 25 000 feet). These trajectory parameters are shown in figure 5 and represent the BET. The BET represents an analysis not subject to any CM aerodynamics or atmospheric effects, in that the BET uses, primarily, guidance-and-navigation data which have been corrected for all known errors and then fitted where possible to available ground-radar data. Details of the trajectory reconstruction can be found in reference 6. The spacecraft position is shown in figure 5(a) in terms of altitude h , longitude Θ_{GD} , and geodetic latitude Φ_{GD} . The spacecraft velocity vector relative to the air is shown in figure 5(b) as a magnitude (total velocity V_A) and as a direction (flightpath angle γ_A and azimuth clockwise from north σ_A). The deceleration load factor shown in figure 5(c) is the accelerometer-sensed deceleration time history divided by the acceleration of gravity at sea level. The dynamic pressure presented in figure 5(d) is that calculated from the onboard pressure measurements. The Mach number and Reynolds number time histories presented in figures 5(e) and 5(f), respectively, are based on an atmosphere that was measured by low-altitude sounding-rockets (up to 180 000 feet) and then extrapolated to 400 000 feet. The atmospheric data (presented in figure 6 as percentage of the 1962 standard atmosphere (ref. 8)) were obtained near the entry trajectory (Eniwetok Atoll, Marshall Islands) in the form of Rawinsonde data (up to 115 000 feet) and Arcasonde data (up to 180 000 feet). These data were analyzed and then extrapolated horizontally using the thermal-wind equations, the geostrophic-wind equations, and the mass-wind equations to provide data along the ground track. These results were extrapolated vertically to 400 000 feet using the temperature structure, the hydrostatic equation, and the equation of state. This method is detailed in reference 9.

PRESENTATION OF RESULTS

The flight aerodynamic data are presented in groups as shown in table I. Aerodynamic angles are shown in figures 7 and 8, aerodynamic force ratios are shown in figures 9 and 10, and aerodynamic force coefficients are shown in figures 11 and 12. These data are compared, where possible and meaningful, with the two sets of data defined in the two sections which follow.

Wind-Tunnel Data

The data, referred to as wind-tunnel data, resulted from an analysis of CM experimental data which was fitted to the specific entry configuration (CM 011) of the Apollo AS-202 mission. The Apollo wind-tunnel testing program data (refs. 2 to 5) were faired with both Mach number and angle of attack to form a set of data consistent among the many test facilities and test conditions. Because no data were obtained in the initial entry high-Mach-number, low-Reynolds-number flight regime, it was necessary to extrapolate preflight data to this region. Modifications were then made to account for certain differences between the flight configuration and the tested models. The protuberances that would affect the aerodynamics can be seen in the spacecraft postflight photographs (figs. 1(a) and 1 (b)). The protuberances and the entry configuration are dimensioned in figure 1(c). The significant effect noted was on the moment coefficients and, consequently, on the trim angles. In addition, because an unsymmetrical configuration results from the variable thickness of the ablative material on the aft heat shield (fig. 1(d)), an analytical approximation of the trim angle of attack was made to account for the effective cant angle between the centerline of the forebody structure and the centerline of the approximated ablative sphere. The approximation of the trim angle of attack was extended to account for the effective offset (measured at the surface of the heat shield) between the respective centerlines. Also, because of reaction-control subsystem (RCS) propellant expenditures, movement of the spacecraft c. g. was significant enough to take into account (table II). The data, thus modified, represent the best prediction of the CM aerodynamic characteristics based on wind-tunnel data.

Wind-Tunnel Data Adjusted to Flight Angle of Attack (Hybrid Data)

In an effort to eliminate the dependence of the wind-tunnel force data on the predicted trim angles, a new set of force data was generated. Flight angle of attack and Mach number as a function of time were combined with wind-tunnel data as a function of test angle of attack and Mach number in order to generate the new force data, which are referred to as hybrid data. (Refer to fig. 13 for an example of the way the hybrid data were obtained.) It is possible to construct an $(L/D)_{RG}$ time history for this mission by interpolating total L/D as a function of the flight calculated α_R and M . The example shown is for $M = 6.0$. These hybrid data, when compared to the wind-tunnel and flight data (table I), are indicated in the figures by a symbol; however, the reader is cautioned that the symbol does not represent individual flight calculations, nor individual wind-tunnel test points. The symbol represents a combination of these. Also, the resultant hybrid aerodynamic parameters are based on the assumption of a symmetrical configuration, which wind-tunnel data have confirmed within the limits of accuracy of the wind-tunnel data.

Factors Influencing the Aerodynamic Data

Several factors which affect each group of data should be noted. A list of these factors is included for reference purposes. The first three factors will affect comparisons of all aerodynamic data, the fourth and fifth factors will affect only the flight aerodynamic ratios and coefficients, and the last factor will affect only the flight

aerodynamic-coefficient data. Quantitative effects of some of these factors are presented in the section on flight-data uncertainties.

Trajectory parameters dependent on definition of atmosphere. - The trajectory parameters that require a knowledge of atmospheric data are Mach number (fig. 5(e)) and Reynolds number (fig. 5(f)), which are calculated with the use of the sounding-rocket data. Because of basic uncertainties in sounding-rocket data, the necessity for an extrapolation procedure, and the possibility of altitude uncertainties in the trajectory data, the flight-Mach-number and flight-Reynolds-number time histories cannot be considered to be as accurate as those measured in the wind tunnels.

Static-versus dynamic-type data. - The ground-facility data, which represent a steady-state condition, indicate that there are flow regions where the aerodynamic trim values undergo considerable changes. In actual flight these regions are traversed very rapidly. That is, before a steady-state trim attitude is established for the flow condition of the static data, the vehicle is in a different flow environment. There are also times when the flight data may reflect a transient response to dynamic conditions encountered in the region of reaction-control-engine firing, in flow regions where negative damping is present, or in the region of the transonic-flow regime.

Untrimmed flight regions. - The data comparison is considered invalid where the atmosphere is too thin to trim the entry vehicle effectively. The effect of the thin atmosphere is reflected in figure 5(d) where there appear two regions of low dynamic pressure. One such region appears during the initial entry phase, and another appears during the skip (Kepler) phase.

Low deceleration regions. - Because the external forces measured by the inertial-platform accelerometers are low where the deceleration load-factor level is less than 0.25g, the flight force data in this region are considered to be invalid. These regions are noted on each time-history plot that includes acceleration data (from initial entry to $t + 4450$ seconds and from $t + 4640$ seconds to $t + 4740$ seconds).

Average force data from flight instrumentation. - The flight force data, in the form of averaged values (as opposed to instantaneous values), are obtained from pulse-integrating pendulous accelerometers which accumulate velocity changes (pulses) over a 2-second interval and then average the pulses.

Dynamic pressure calculated from flight measurements. - The time history of dynamic pressure used to calculate the flight force coefficients was obtained using surface-pressure flight measurements taken on the face of the aft heat shield (in the region of the stagnation point). This method of obtaining flight coefficients was considered to give a more realistic time history (i. e., independent of altitude and other uncertainties) than did the extrapolation of sounding-rocket data over to, and up through, the altitude region of interest. The calculation was based on the fact that the ratio of free-stream dynamic pressure q_∞ to measured stagnation pressure was taken to be a constant. (This correlation is treated in more detail in ref. 10.) The value of the constant was taken to be slightly higher than the value suggested in the reference. This was done so that the flight coefficient data can be considered valid, within the limits of the reference, down to transonic Mach numbers. Also, in regions of low dynamic pressure, the accuracy of this calculated parameter became poor, as was reflected in the flight coefficient data.

RESULTS AND DISCUSSION

Aerodynamic Angles

The aerodynamic angles α , β , Φ_A , and α_R that relate the free-stream velocity vector to the body axes are presented as time histories in figure 7. The total angle of attack α_R is repeated in figure 8 as a function of Mach number. The flight data show that the vehicle is not aerodynamically trimmed at the initial entry point, where the air is thin, but that the vehicle begins to seek a general trim condition shortly after initial entry (near $t + 4390$ seconds, $M \approx 31.0$). The data scatter in the region from $t + 4410$ seconds ($M \approx 31.0$) to $t + 4480$ seconds ($M \approx 28.0$) is also influenced by firing the reaction-control engines to perform the planned 180° roll maneuver (from lift-vector down to lift-vector up). The data show a reasonably firm steady-state trim condition when the roll maneuver is completed. During the skip (Kepler) phase the low density of the surrounding air allows the spacecraft to oscillate with higher amplitudes about the aerodynamic trim attitude. When the spacecraft reattains a steady-state trim condition, the values for flight total angle of attack (fig. 7(d)) oscillate within a band of less than 2° . The flight data, which show an essentially linear decrease of trimmed α_R during the hypersonic portion of the entry, are approximately 3.5° to 1° above the almost constant wind-tunnel data. (Compare a flight α_R of approximately 162.5° to wind-tunnel data of 159.0° at $t + 4480$ seconds ($M \approx 28.0$). Also compare a flight α_R of approximately 160.3° to wind-tunnel data of 159.3° at $t + 5030$ seconds ($M \approx 6.0$.) Below $M \approx 6.0$ the flight α_R data follow the trend of the wind-tunnel data, down to $t + 5124$ seconds ($M \approx 1.35$), staying within 2° of the wind-tunnel data. The flight data then veer off, showing much higher trim angles down to $t + 5180$ seconds ($M \approx 0.6$). The role of the previously cited influencing factors, in the region of poor agreement, may be clarified by a comparison of the data from $t + 5124$ seconds to $t + 5180$ seconds (fig. 7(d)) with this same data region as plotted against Mach number (fig. 8).

Aerodynamic Coefficient Ratios

The amount of down-range (longitudinal) and cross-range (lateral) maneuver capability of the entry configuration is a function of the lift-to-drag and side-force-to-drag ratios in, and perpendicular to, the orbital plane, respectively. These force ratios result from banking the spacecraft so that one portion of the resultant, or total, lift-to-drag ratio $(L/D)_{RG}$ is in the orbital plane (the portion $(L/D)_G$), and another portion $(Y/D)_G$ is perpendicular to the orbital plane. Figure 9(a) for $(L/D)_G$ depicts very clearly the initial negative-lift entry and the 180° roll maneuver, followed by an essentially positive full-lift attitude for the remainder of the entry. The plot of $(Y/D)_G$ in figure 9(b) indicates that the onboard guidance system detected a cross-range error during the initial portion of the flight and was attempting to correct for the error by commanding the appropriate bank angle.

The total lift-to-drag ratio is presented in figure 9(c) as a function of time and in figure 10 as a function of Mach number. Also in figures 9(c) and 10, the total lift-to-drag ratio is compared with the wind-tunnel data and the hybrid data. The trend of the flight $(L/D)_{RG}$ is similar to, and consistent with, that of the flight α_R . The data start with a trimmed total L/D of approximately 0.27 at the beginning of entry (wind-tunnel L/D is 0.05 (18 percent) higher), and increase to a total L/D of approximately 0.31 at $M \approx 6.0$ (wind-tunnel L/D is 0.007 (2 percent) higher). From $M \approx 6.0$ down to $M \approx 1.35$ the data show fair agreement (within about 12 percent); then, as with the α_R data comparisons, from $M \approx 1.35$, there are large differences between the flight data and the wind-tunnel data. As explained in the previous section, these differences appear to be more reasonable as a function of Mach number (fig. 10).

The comparison of these two sets of data for the entire flight shows that from $M \approx 23$ down to $M \approx 1.35$ (approximately 65 percent of the entry time) the flight total L/D is within the stated preflight uncertainty (± 0.04) in the predicted data. The wind-tunnel data adjusted to flight α_R (hybrid data) follow the flight calculated data very closely for the entire entry, indicating that the high values of wind-tunnel L/D are due to poor trim predictions and not due to poor wind-tunnel resultant force data. (Refer to the presentation of results section for factors that may influence the comparisons.)

Aerodynamic Body Axis Force Coefficients

The coefficient-ratio data of the preceding section indicate that the predictions of the trim angle caused the difference between the levels of the flight data and the wind-tunnel data. Therefore, the wind-tunnel data adjusted to the flight calculated angle of attack (the hybrid data) give a more valid comparison with the flight calculated data. The levels of the wind-tunnel coefficients obtained from the predicted α_R are shown on the figures for completeness only. Also, the regions of poor flight coefficient data around the initial entry and the skip phase have been extended because of the decreased accuracy of the flight calculated dynamic pressure.

The C_A comparison between flight and hybrid data in figure 11(a) shows a region of fair agreement at the hypersonic Mach numbers. (Hybrid data are a maximum of about 12 percent above flight data.) The agreement becomes good (about 5-percent difference) at some time after the skip phase (at approximately $t + 4850$ seconds ($M \approx 17.4$)). The difference in the hybrid data increases to as much as 31 percent below flight data in the lower Mach number region (below $M \approx 6.0$, $t + 5030$ seconds) with both sets of data following the same trend. The low magnitude and scatter of the total normal-force-coefficient data in figure 11(b) make a similar comparison for $C_{N,R}$ difficult. In general, however, the flight data and the hybrid data show fair agreement (carried down to the transonic Mach numbers) between the mean levels, with scatter in the data varying by as much as 15 percent.

The flight calculated data for C_Y and C_N presented in figures 11(c) and 11(d) show these small force coefficients to be of the same order of magnitude. This is inconsistent with the levels of magnitude expected of these coefficients when the relative

magnitude of the aerodynamic angles α and β are considered. That is, the wind-tunnel data show the force coefficient slopes, C_Y with angle of sideslip β and C_N with angle of attack α , to be equal within the accuracy of the data. Since the angle of sideslip (fig. 7(b)) and the angle of attack (fig. 7(a)) are not of the same magnitude, the coefficients C_Y and C_N should not be of the same magnitude (C_Y is two to three times higher than was expected, and C_N is about two-thirds of the expected level).

This inconsistency is unexplained at present, other than by consideration of the factors presented in the presentation of results section.

As evidenced by the preceding comparisons, the hybrid aerodynamic data give the best representation of the body axis coefficients for several reasons. The hybrid $(L/D)_{RG}$ data (fig. 9(c)) agree closely with the flight calculated data, signifying that the flight calculated forces agree closely with the measured wind-tunnel forces, when both use a common angle of attack. The disagreement of the coefficient data is largely a result of the uncertainty in the calculated values of dynamic pressure q_∞ used for the flight coefficients. The hybrid data are not affected by this calculation.

Aerodynamic Ground-Relative Force Coefficients

Aerodynamic force coefficients relative to the ground are presented in figure 12. The regions of poor flight coefficient data are again extended as were the body coefficient data. The coefficients $C_{L,G}$ and $C_{Y,G}$ in figures 12(a) and 12(b) are similar to the coefficient ratios relative to the ground presented in figures 9(a) and 9(b) in that $C_{L,G}$ and $C_{Y,G}$ reflect the total lift-vector attitude of the vehicle (with respect to the orbital plane) as obtained through commands from the guidance and control system.

In the hypersonic region above the skip phase, the hybrid drag coefficient (fig. 12(c)) is approximately 11 percent (maximum) above the flight data. After the skip phase and down to $M \approx 6.0$, there is good agreement between hybrid data and flight data. (Hybrid data are as much as 4 percent above flight data.) Below $M \approx 6.0$, there is poor agreement between flight data and hybrid data (with the hybrid data as much as 27 percent below flight data).

The hybrid and flight total lift-coefficient data of figure 12(d) show fair to good agreement at the hypersonic Mach numbers (12- to 13-percent differences), very good agreement after the skip region (3 percent (maximum)), and poor agreement (up to 26 percent) below $M \approx 6.0$ ($t + 5030$ seconds), as did the C_A and $C_{D,G}$ comparisons.

As in the preceding section, the disagreement between the two sets of data can be attributed largely to the use of flight calculated dynamic pressures to obtain the flight coefficient. The hybrid data are considered to be the most reliable source of these aerodynamic coefficients.

Flight-Data Uncertainties

The effect of uncertainties in several input parameters was determined by entering them in the flight-data analysis program as constant increments, added to or subtracted from the nominal input quantities. The magnitudes used were arbitrary; however, they were either representative or conservative. Actually, most of the uncertainties considered were time-variant. The changes (delta values) from the nominal calculated values of several selected aerodynamic parameters have been determined, as have α_R root-sum-square (rss) delta values. Only positive uncertainties were shown because the negative values were essentially mirror images. For the total-angle-of-attack calculation, uncertainties of $\pm 0.5^\circ$ were taken in each of the inertial-platform gibal angles, uncertainties of ± 100 ft/sec were taken in velocity, and uncertainties of $\pm 0.5^\circ$ were taken in both latitude and longitude. (The results of this analysis are shown in figures 14(a) and 14(b) with sufficient data plotted to show trends.) The changes caused by the separate uncertainties in figure 14(a) show the total angle of attack to be affected predominantly by the uncertainty in the pitch gibal angle Θ of the inertial platform, and to a smaller extent by the yaw and roll gibal angles, Ψ and Φ , respectively. The pitch gibal angle Θ has greater effect on α_R because the body X-Z plane and the inertial-platform X-Z plane were nearly coincident during entry.

The uncertainties in spacecraft position also had a considerable effect. For the essentially full-lift entry trajectory, the body X-Z plane was also close to the geodetic $X_{GD}-Z_{GD}$ plane. This was reflected in the relative effects of longitude Θ_{GD} and geodetic latitude Φ_{GD} on the total angle of attack α_R . The velocity uncertainty had no effect on α_R and therefore is not shown on the figure. The rss delta values for α_R (fig. 14(b)) were less than 1° for the entire entry.

For the coefficient program, uncertainties were taken in the platform accelerometer data that represented ± 2 pulses in the accumulation register (± 0.1919 ft/sec²), ± 100 ft/sec in velocity, $\pm 0.04^\circ$ in flight-path angle, $\pm 0.05^\circ$ in azimuth, and an assumption of ± 3 percent of full-scale instrumentation in determining the onboard pressures. (The results of this analysis are represented in figures 14(c) to 14(e).) The uncertainties input for V_A , γ_A , and σ_A had negligible effect on the coefficients and ratios for V_A , γ_A , and σ_A , and therefore, these uncertainties are not plotted in figures 14(c) and 14(d). In figure 14(c) the coefficient ratios are seen to be affected predominantly by the inertial-platform Y- and Z-axis accelerations $A_{y,p}$ and $A_{z,p}$.

As mentioned previously, the body axis coefficient delta values shown in figure 14(d) reflect the close alignment of the inertial platform with the body axis system. Resulting uncertainties in C_A are very low, but the uncertainties in C_Y and C_N are appreciable as compared to the nominal value of the respective coefficients. Figure 14(e) shows the uncertainty in all coefficient data (at any selected time during re-entry) caused by an uncertainty of 3 percent of full scale in the flight-measured

pressures. The assumed uncertainty shown in figure 14(e) is considered to be conservative, but it does indicate very clearly the areas where the flight coefficient data could be subject to large errors.

CONCLUDING REMARKS

The aerodynamic characteristics of the Apollo entry configuration (the command module) have been calculated using flight data which were obtained from the inertial platform in the form of accelerations and inertial attitudes. The results have been compared with wind-tunnel trimmed aerodynamic data and with wind-tunnel data adjusted to flight angle of attack (the hybrid data). Factors are pointed out which influence the calculated flight data and the comparisons of flight data with other data. Also pointed out are the effects on the flight data of several input uncertainties. The following should be noted:

1. At the point along the trajectory where a steady-state trim condition is reached (near a Mach number of approximately 28.0), the predicted wind-tunnel data show a total angle of attack which is 3.5° below the flight calculated value of 162.5° and show a total lift-to-drag ratio which is 18 percent above the flight value of approximately 0.27. Flight total angle of attack and total lift-to-drag ratio are essentially linear along the trajectory to a Mach number of approximately 6.0 where the wind-tunnel data show a total angle of attack which is approximately 1° below the flight value of 160.3° and show a total lift-to-drag ratio which is 2 percent above the flight value of approximately 0.31. (Wind-tunnel total angle of attack and total lift-to-drag ratio are approximately constant.) Fair agreement is shown (total angle-of-attack differences up to 2° and total lift-to-drag ratio differences up to 12 percent) from a Mach number of approximately 6.0 down to a Mach number of approximately 1.35 and below a Mach number of approximately 0.6, with a region of poor agreement from a Mach number of approximately 1.35 to a Mach number of approximately 0.6.

2. The comparison between the flight calculated total lift-to-drag ratio and the wind-tunnel total lift-to-drag ratio shows that this important aerodynamic parameter is within the stated preflight uncertainty band (± 0.04) from a Mach number of approximately 23.0 to a Mach number of approximately 1.35 (approximately 65 percent of the entry time).

3. The good agreement between the total lift-to-drag ratio from flight calculations and the total lift-to-drag from hybrid data indicates that the wind-tunnel trim-angle prediction, and not the wind-tunnel force-coefficient data, was the cause of the higher prediction of total lift-to-drag ratio.

4. The hybrid data are believed to give the best representation of the aerodynamic coefficients because of the good agreement mentioned in total lift-to-drag ratio, and because they are not subject to the flight dynamic-pressure calculations. Comparison of the hybrid data with flight calculated values shows the aerodynamic coefficients for axial force, drag force, and total lift to be in fair to good agreement (maximum differences of 13 percent to differences of less than 3 percent) down to a Mach number of approximately 6.0, with poor agreement (up to 36-percent differences) below this

Mach number. The flight total normal-force coefficient is very scattered, showing fair agreement (varying up to 15 percent) with hybrid data for the entire flight.

Manned Spacecraft Center
National Aeronautics and Space Administration
Houston, Texas, July 13, 1967
914-50-89-00-72

REFERENCES

1. Moseley, William C., Jr.; and Martino, Joseph C.: Apollo Wind Tunnel Testing Program — Historical Development of General Configurations. NASA TN D-3748, 1966.
2. Moseley, William C., Jr.; Moore, Robert H., Jr.; and Hughes, Jack E.: Stability Characteristics of the Apollo Command Module. NASA TN D-3890, 1967.
3. Jorgensen, Leland H.; and Graham, Lawrence A.: Predicted and Measured Aerodynamic Characteristics for Two Types of Atmosphere-Entry Vehicles (U). NASA TM X-1103, 1965.
4. Neal, Luther, Jr.: An Exploratory Investigation at a Mach Number of 6.9 into the Use of Aerodynamic Controls for Modulating the Lift-Drag Ratio of an Apollo Type Configuration (U). NASA TM X-816, 1963.
5. Wilkinson, D. B.: Hypersonic Shock Tunnel Tests of the .05 Scale Apollo Force Model FS-8 (U). Cornell Aeronautical Laboratory Report AA-1712-W-1. (Prime NASA Apollo Contract NAS 9-150), Oct. 1962.
6. Anon.: Apollo AS-202 Trajectory Reconstruction. Vol. I: Analysis. TRW Systems. TRW Note 66-FMT-257. (Prep. for MPAD, NASA/MSC under NAS 9-4810, Project Apollo Task MSC/TRW A-50), Nov. 1966.
7. Anon.: AS-202 Guidance and Navigation Error Analysis — Final Report. TRW Systems. (Prep. for NASA/MSC under NAS 9-4810, Project Technical Report Task ASPO-38), May, 1967.
8. Anon.: U.S. Standard Atmosphere, 1962. COESA, 1962.
9. Pitts, David E.; and Carter, Patricia C.: High-Altitude Atmospheric Measurements for the Reentries of Gemini 6 and 7. NASA TM X-58003, 1966.
10. Lewis, Clark H.; and Burgess, E. G., III: Altitude-Velocity Table and Charts for Imperfect Air. AEDC-TDR-64-214 (Prep. under contract AF40(600)-1000 by ARO, Inc., Contract Operator of AEDC, Arnold Air Force Station, Tenn.), Jan. 1965.

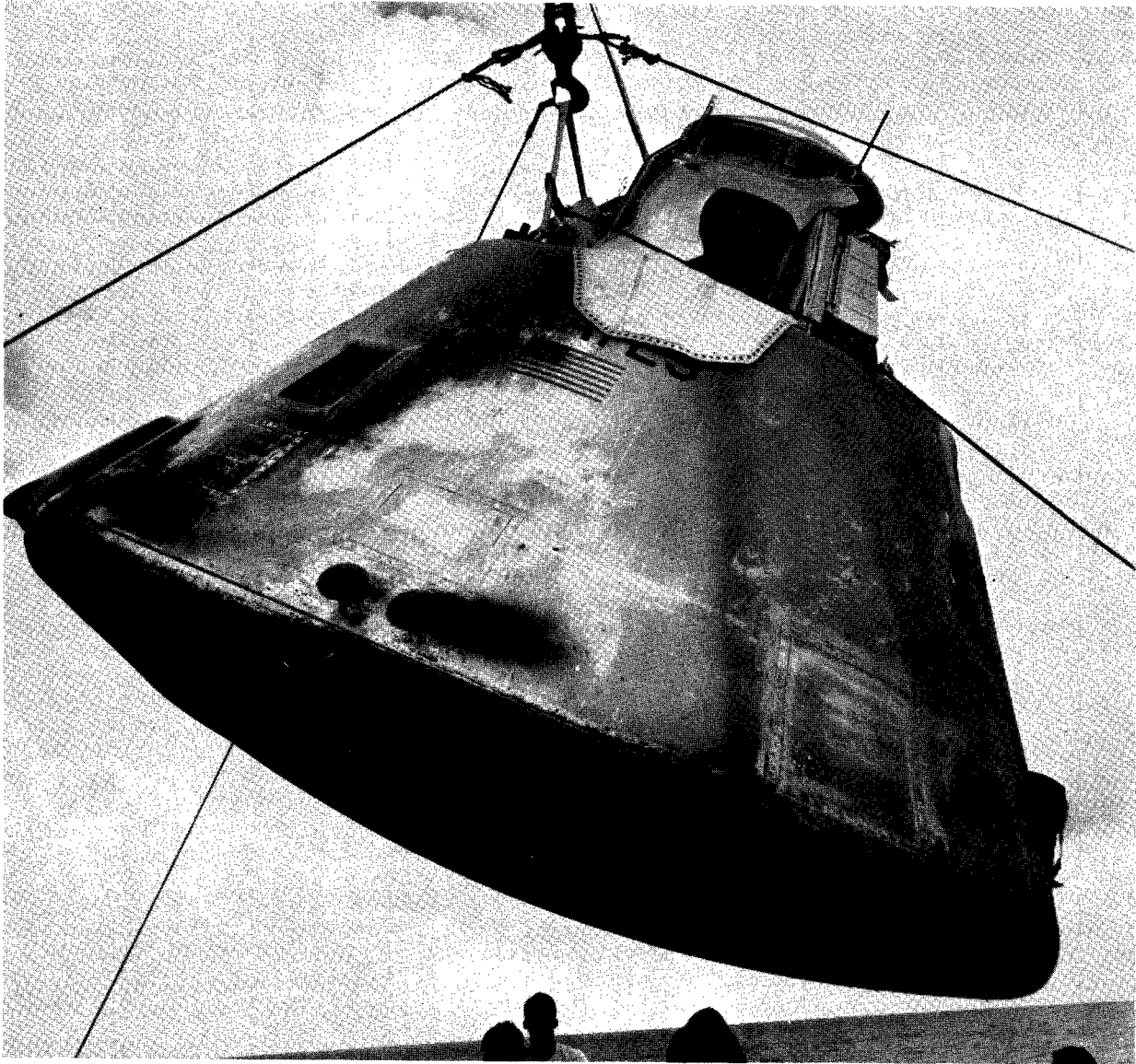
TABLE I. - SOURCES OF AERODYNAMIC DATA PRESENTED

| Figure | Aerodynamic parameter | Flight data | Wind-tunnel data | Wind-tunnel data adjusted to flight angle of attack (hybrid data) |
|--------|-------------------------|-------------|------------------|---|
| 7(a) | α versus t | X | | |
| 7(b) | β versus t | X | | |
| 7(c) | Φ_A versus t | X | | |
| 7(d) | α_R versus t | X | X | |
| 8 | α_R versus M | X | X | |
| 9(a) | $(L/D)_G$ versus t | X | | |
| 9(b) | $(Y/D)_G$ versus t | X | | |
| 9(c) | $(L/D)_{RG}$ versus t | X | X | X |
| 10 | $(L/D)_{RG}$ versus M | X | X | X |
| 11(a) | C_A versus t | X | X | X |
| 11(b) | $C_{N,R}$ versus t | X | X | X |
| 11(c) | C_Y versus t | X | | |
| 11(d) | C_N versus t | X | | |
| 12(a) | $C_{L,G}$ versus t | X | | |
| 12(b) | $C_{Y,G}$ versus t | X | | |
| 12(c) | $C_{D,G}$ versus t | X | X | X |
| 12(d) | $C_{L,RG}$ versus t | X | X | X |

TABLE II. - MOVEMENT OF SPACECRAFT CENTER OF GRAVITY
 BASED ON REACTION-CONTROL SUBSYSTEM FUEL USAGE

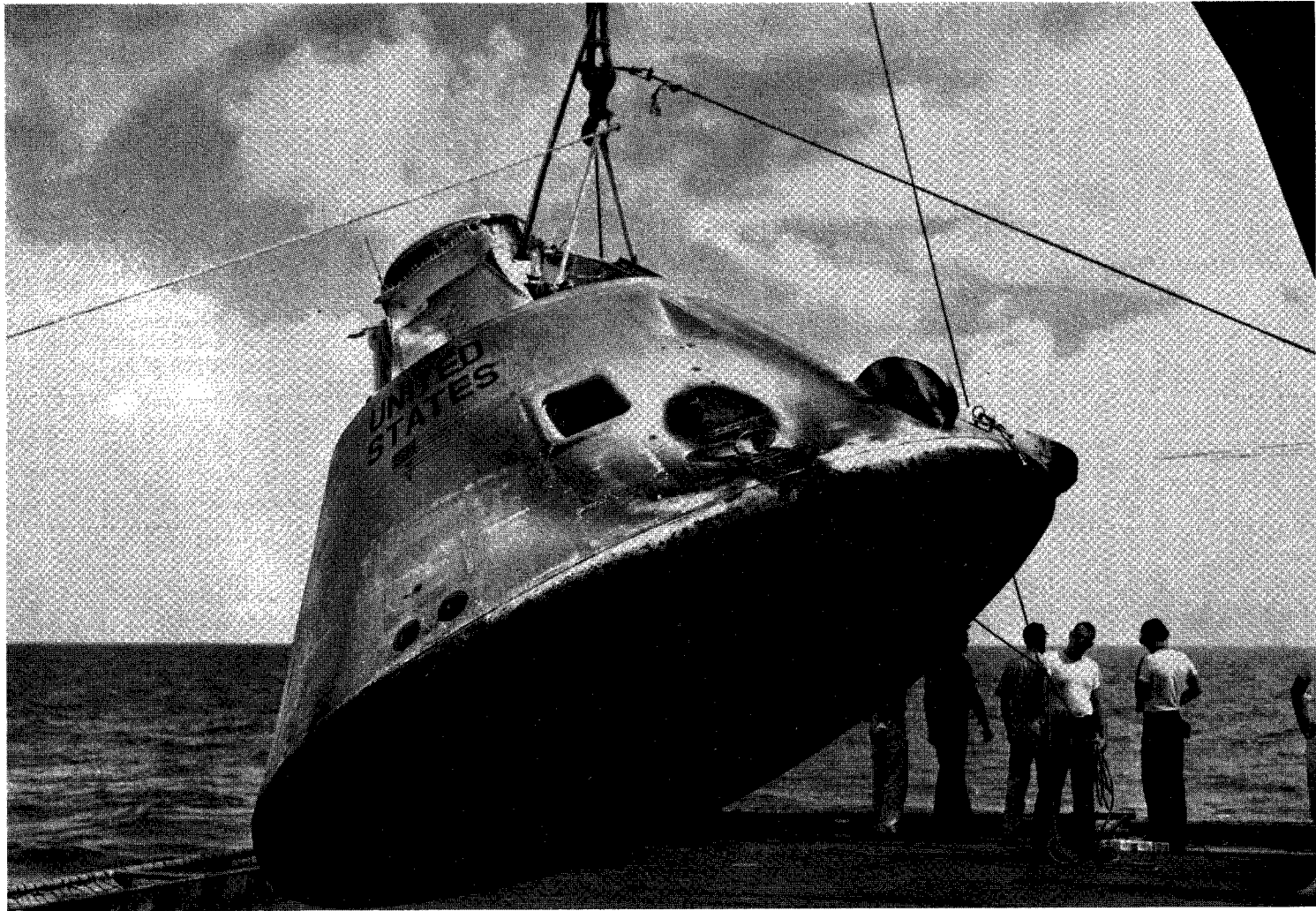
| Mach number, M | Center of gravity, in. (a) | | |
|-------------------|-------------------------------|--------|--------|
| | X-axis | Y-axis | Z-axis |
| 31.0 | 1040.30 | 0.60 | 5.20 |
| 6.0 | 1040.37 | .67 | 5.07 |
| 4.0 | 1040.40 | .67 | 5.03 |
| 3.0 | 1040.43 | .67 | 4.99 |
| 2.4 | 1040.46 | .68 | 4.97 |
| 2.0 | 1040.48 | .68 | 4.95 |
| 1.65 | 1040.49 | .68 | 4.93 |
| 1.35 | 1040.51 | .68 | 4.90 |
| 1.2 | 1040.53 | .68 | 4.89 |
| 1.1 | 1040.54 | .69 | 4.88 |
| .9 | 1040.57 | .69 | 4.84 |
| .7 | 1040.61 | .69 | 4.80 |
| .4 | 1040.70 | .70 | 4.70 |

^aCenters of gravity are in the NASA reference system. The longitudinal reference (body X-axis) has an origin 1000 inches below the tangency line of the command module substructure mold line.



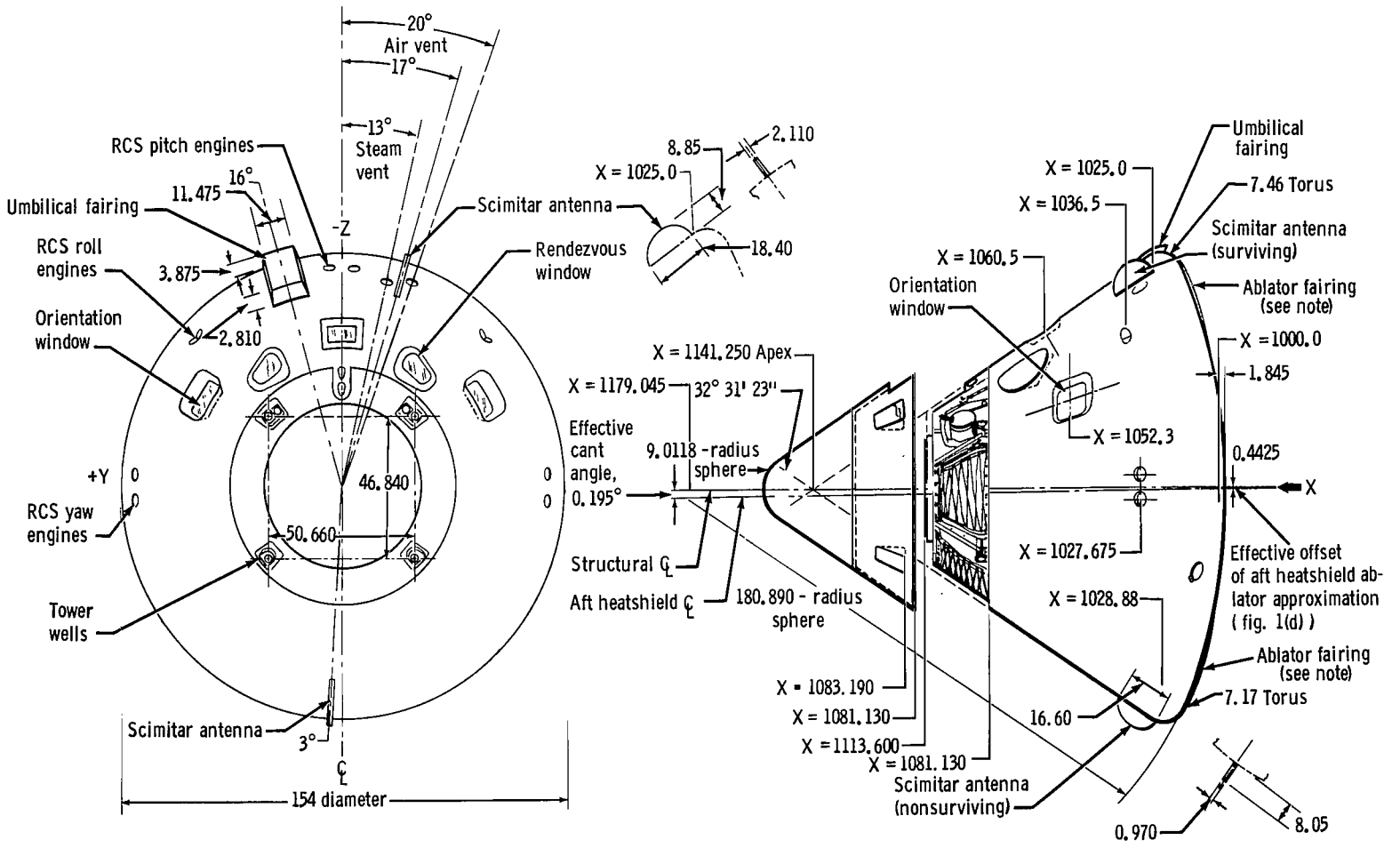
(a) Photo of spacecraft aboard recovery ship USS Hornet looking into body +Y-axis.

Figure 1. - Apollo command module CM 011 entry configuration.



(b) Photo of spacecraft aboard recovery ship USS Hornet looking into body -Y-axis to -Z-axis.

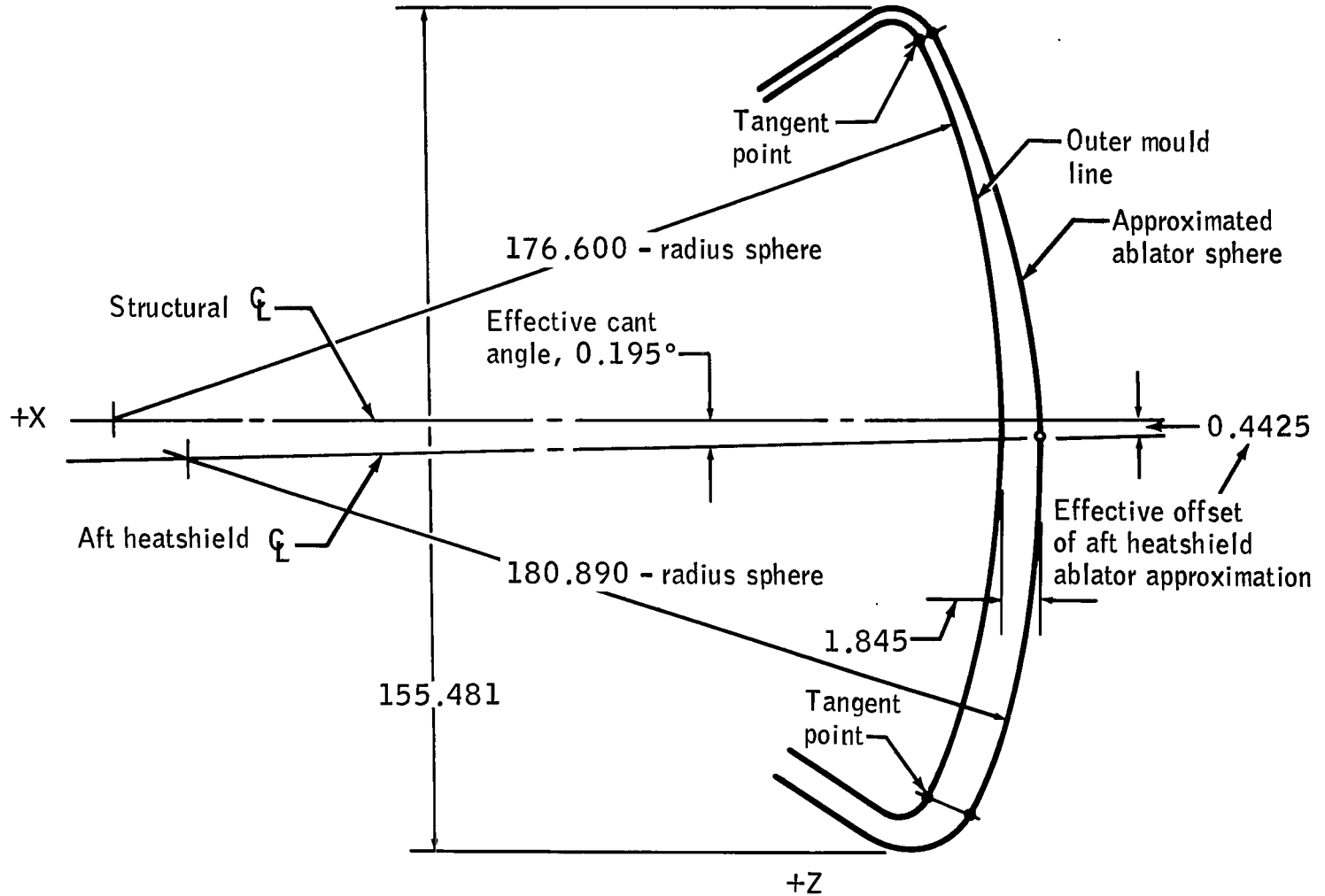
Figure 1. - Continued.



Note: The existing preflight wind tunnel data reported herein did not include the effects of the ablator fairings around the six evenly-spaced shear and compression pads that are located on the aft heatshield.

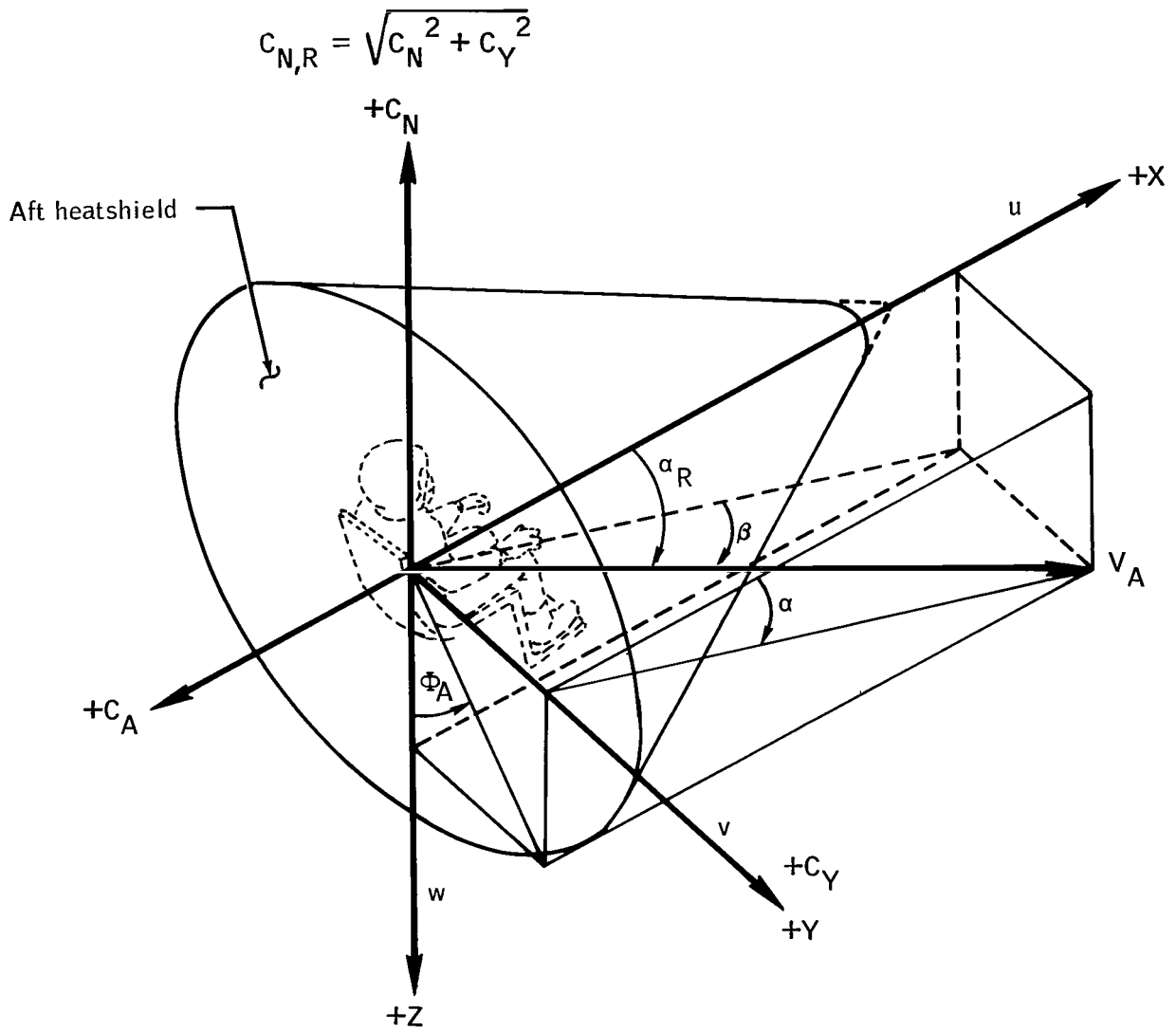
(c) Command module CM 011 dimensions, full-scale linear dimensions, in.

Figure 1. - Continued.



(d) Command module CM 011 aft heat-shield ablator (ablator thickness exaggerated for clarity).

Figure 1. - Concluded.



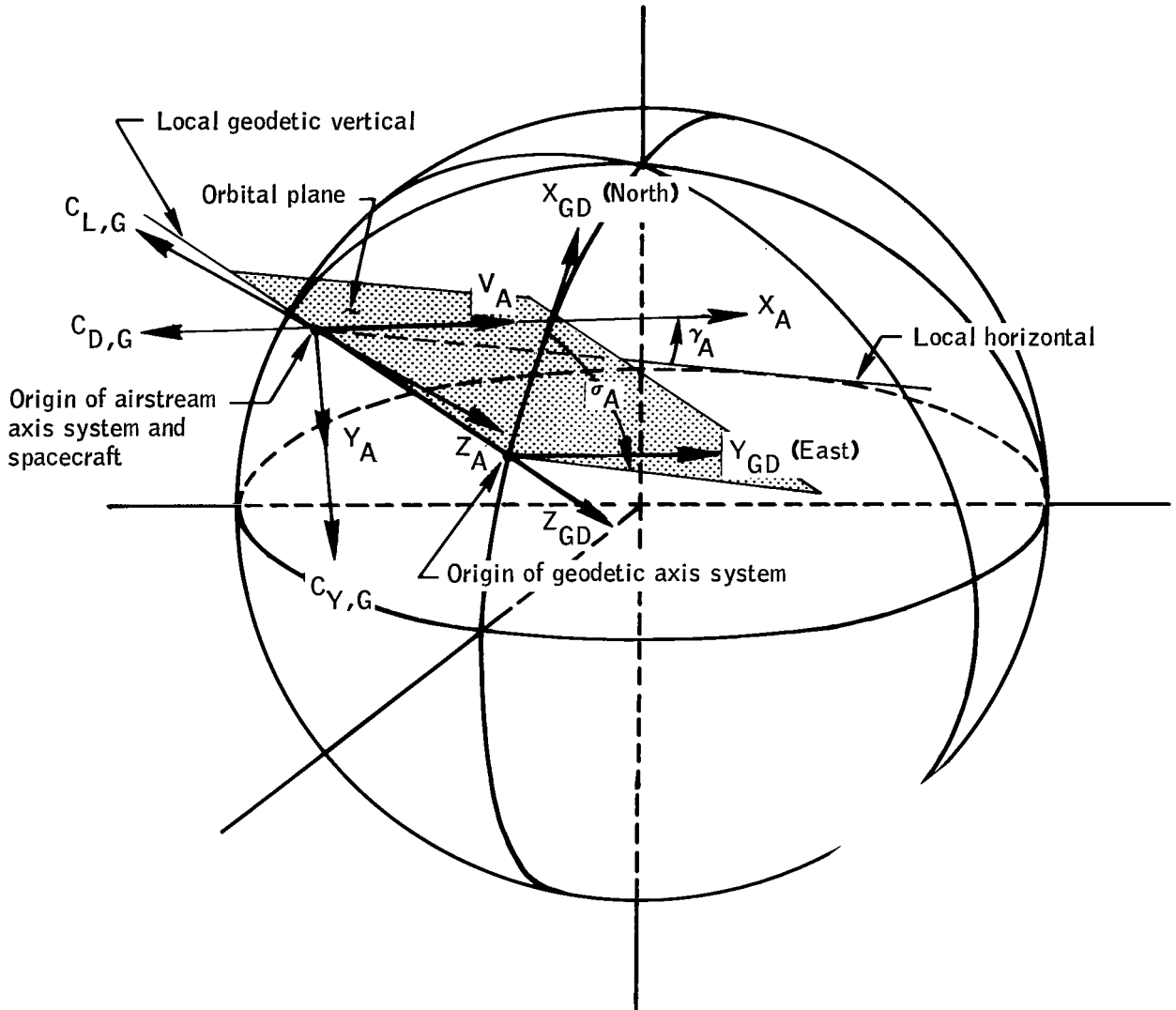
(a) Body axis system showing positive directions of aerodynamic angles and aerodynamic body force coefficients.

Figure 2. - Definition of axis systems.

$$(L/D)_G = C_{L,G}/C_{D,G}$$

$$(Y/D)_G = C_{Y,G}/C_{D,G}$$

$$(L/D)_{RG} = \sqrt{C_{L,G}^2 + C_{Y,G}^2}/C_{D,G}$$



(b) Geodetic and airstream axis systems showing positive directions of aerodynamic coefficients, axes, and angles relative to the ground.

Figure 2. - Concluded.

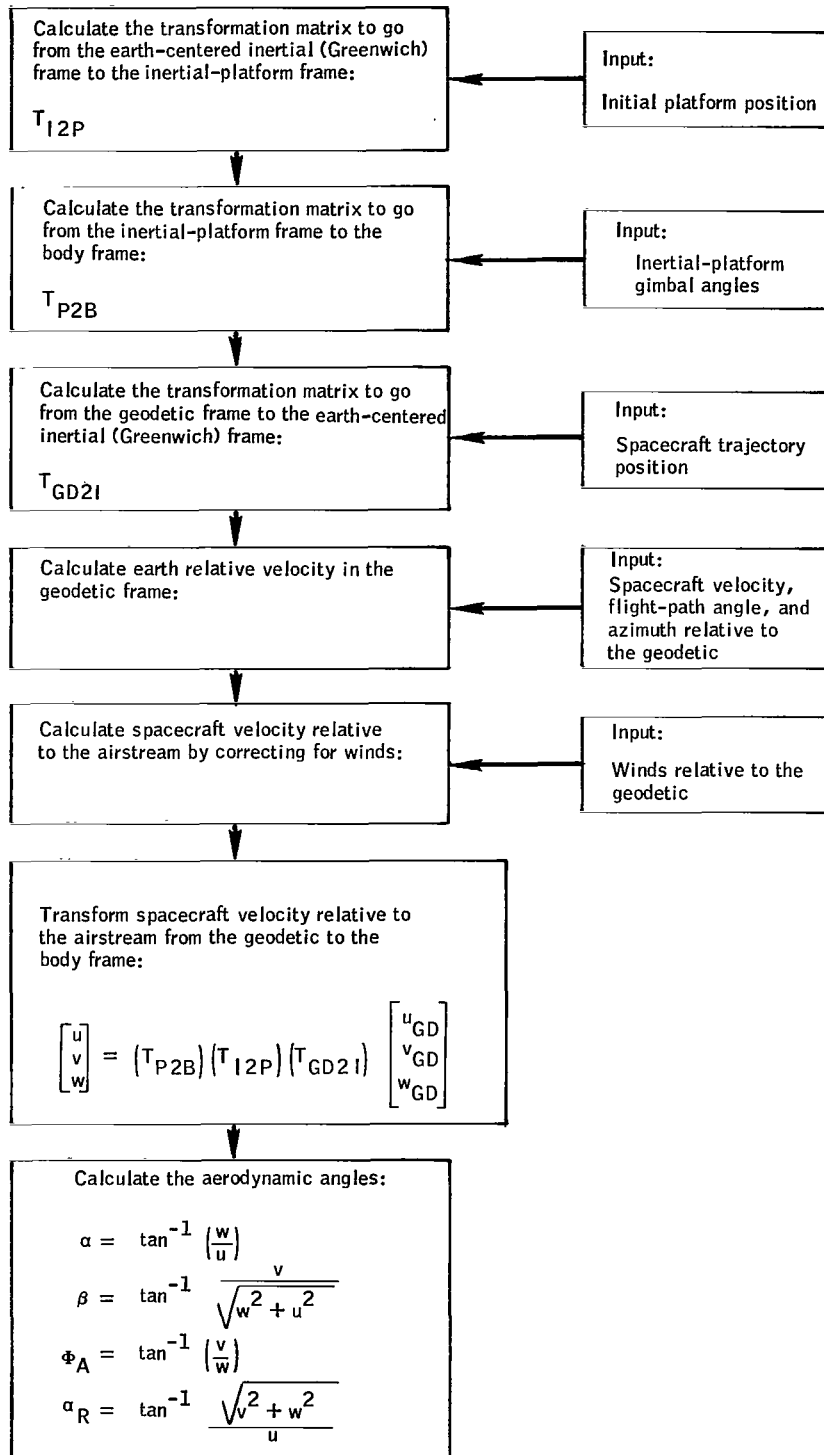


Figure 3. - Angle-of-attack program flow diagram.

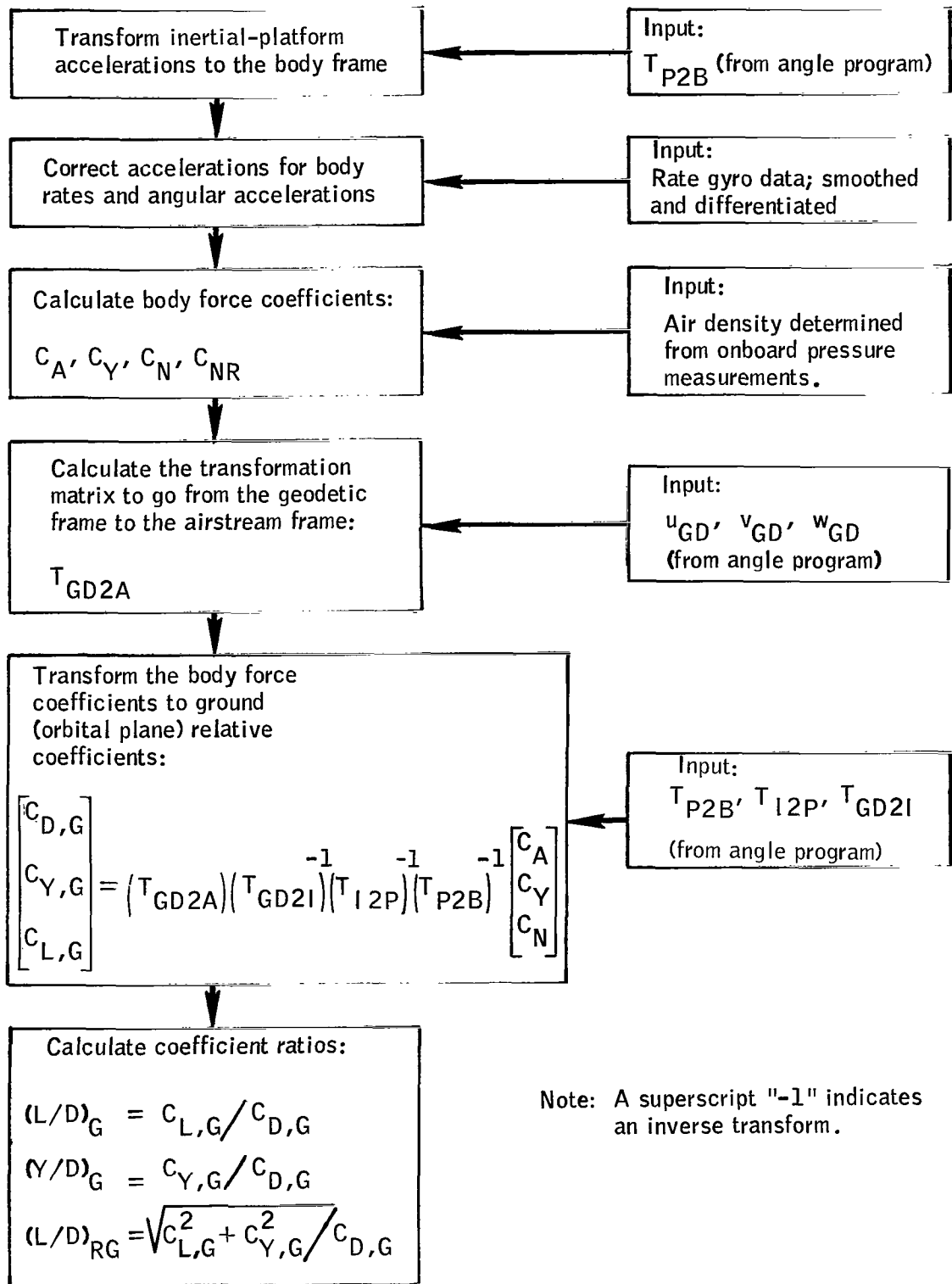
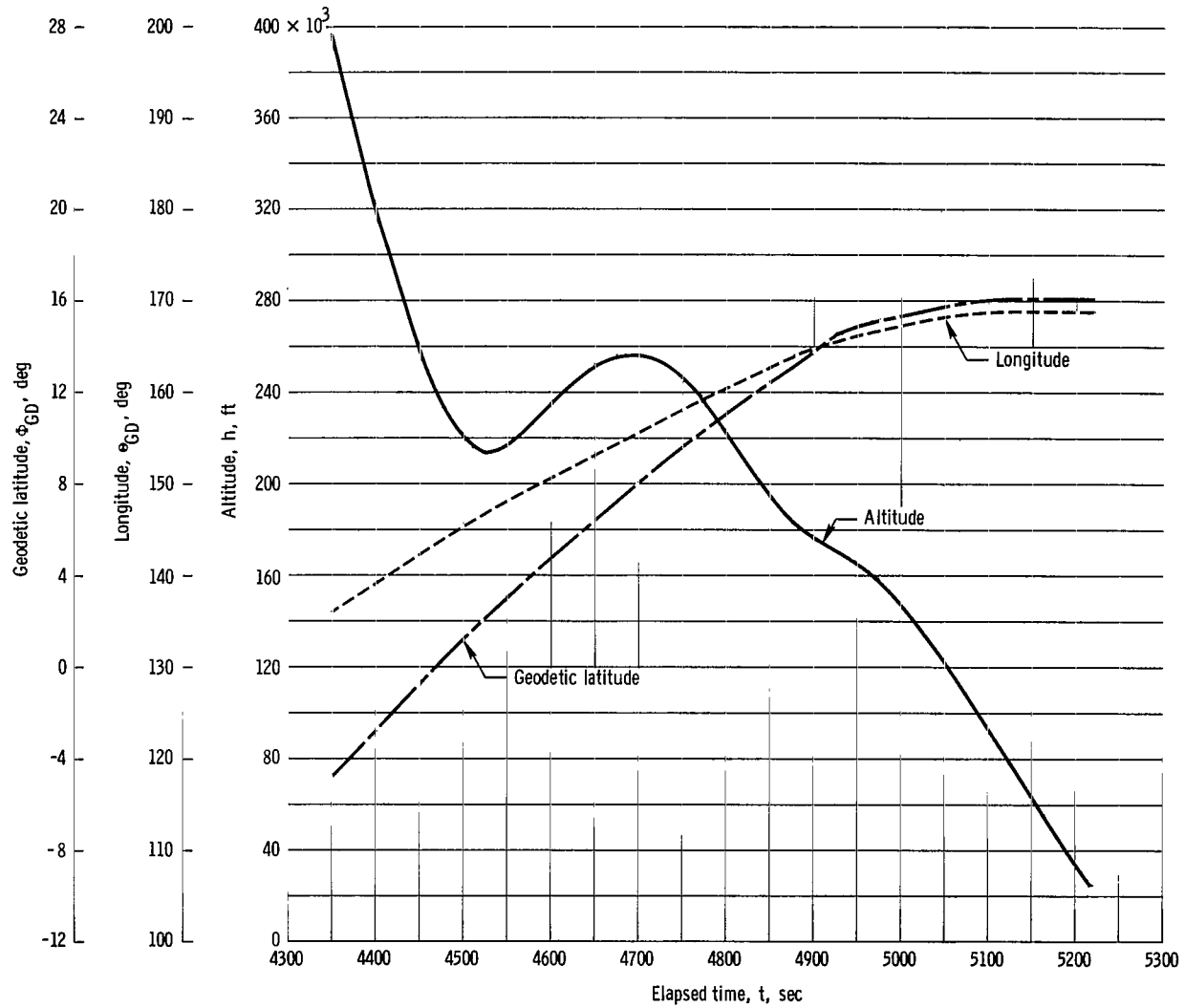
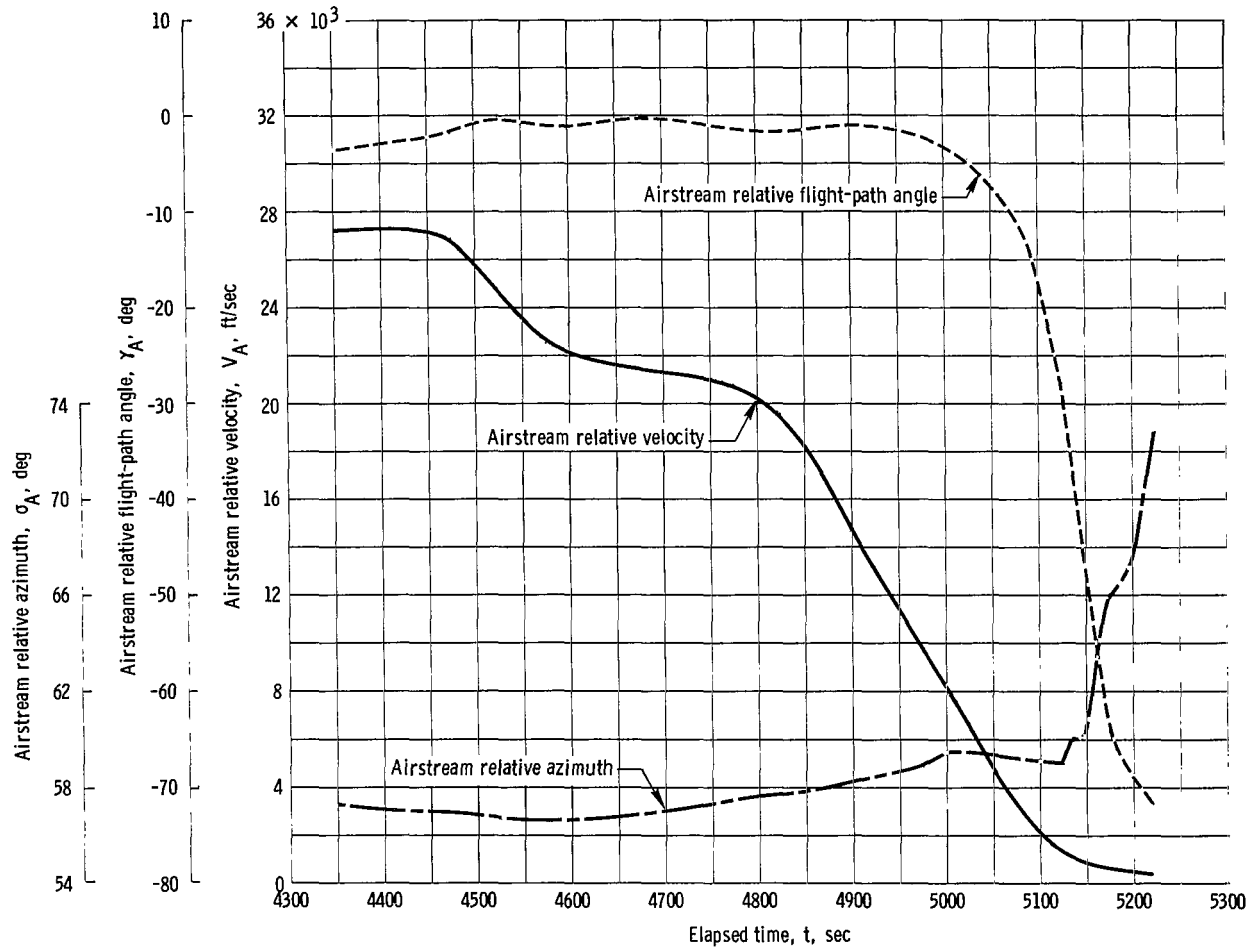


Figure 4. - Aerodynamic-coefficient program flow diagram.



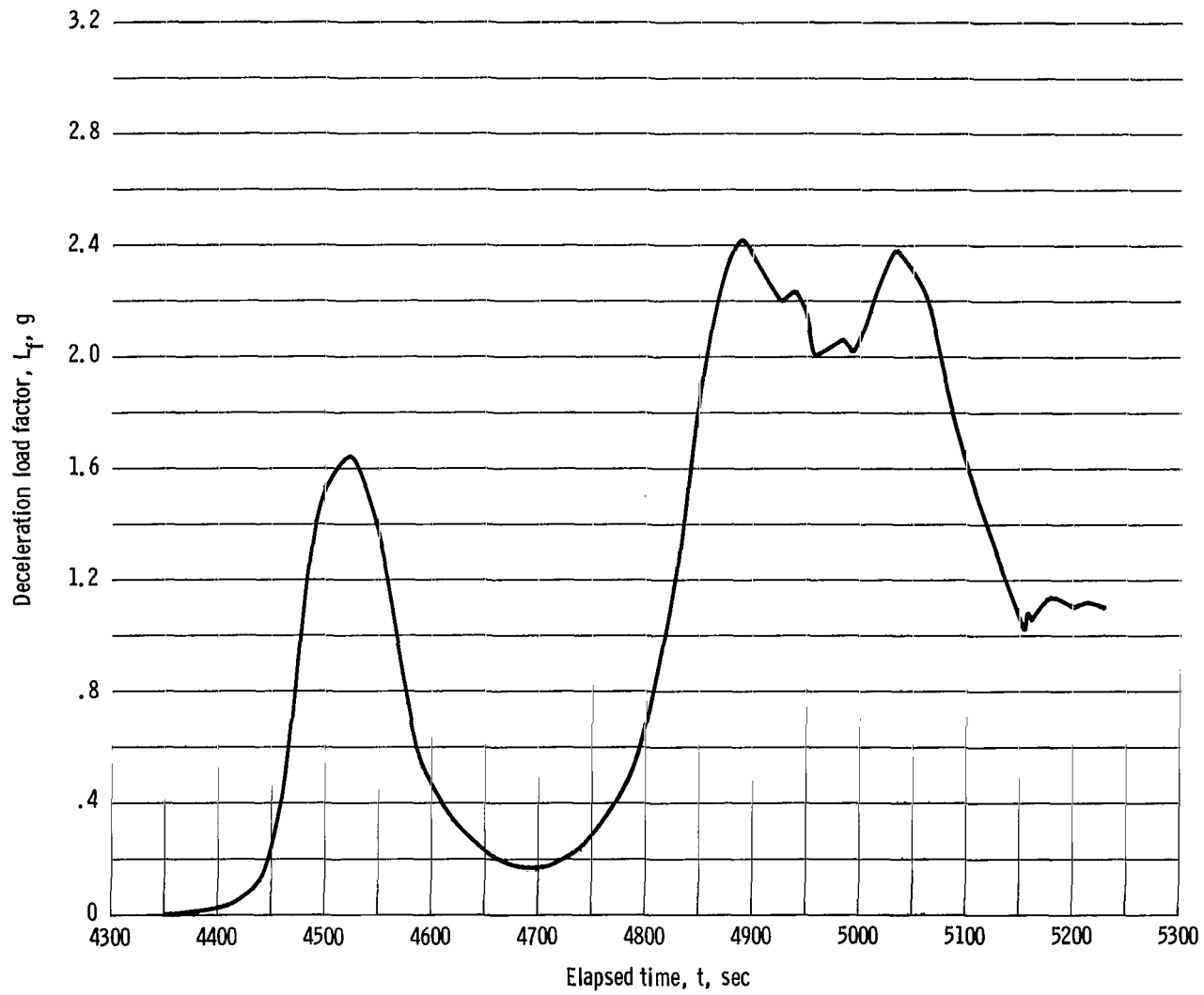
(a) Altitude h , longitude Θ_{GD} , and geodetic latitude Φ_{GD} .

Figure 5. - Time histories of trajectory parameters for reentry phase, Mission AS-202.



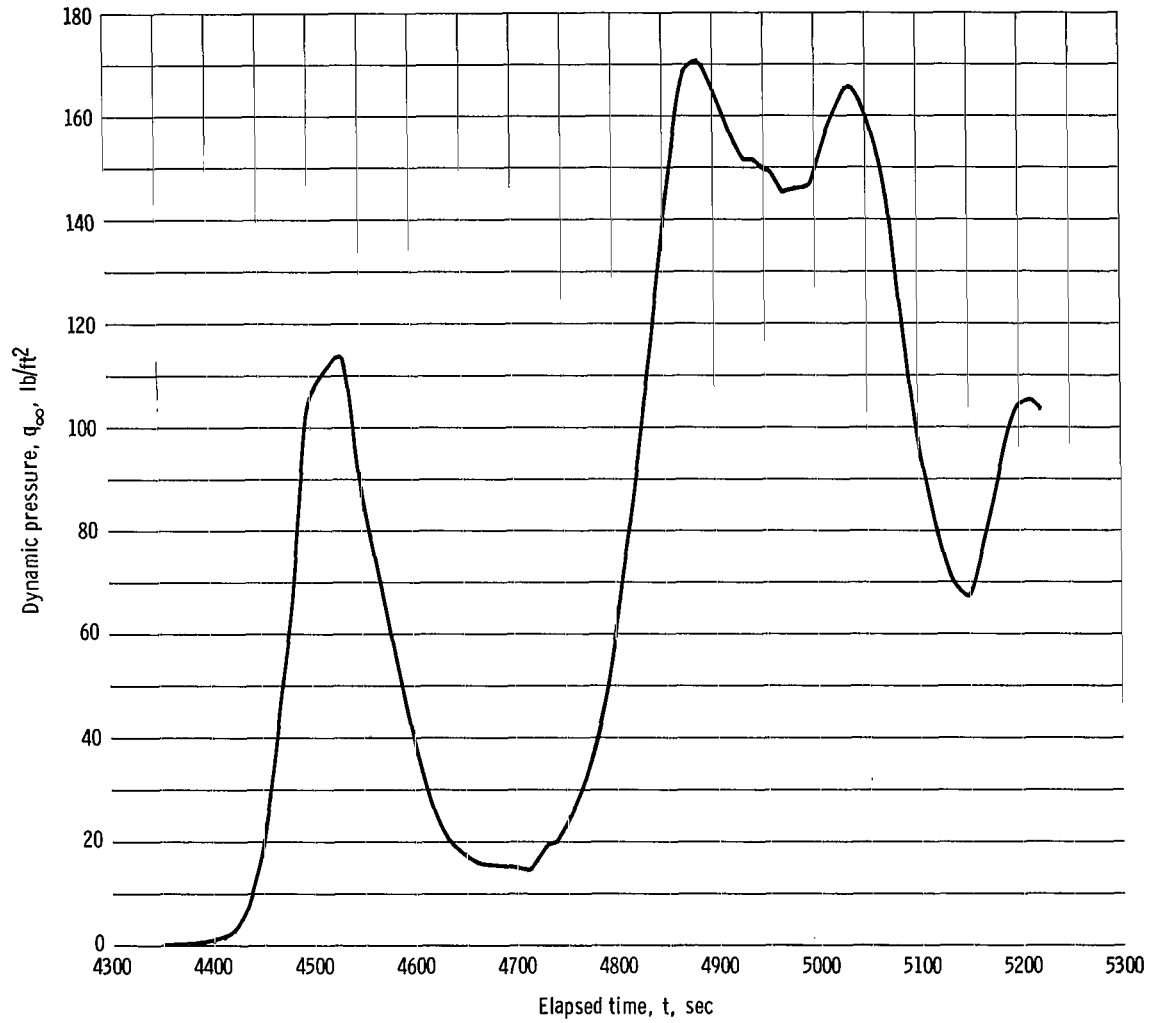
(b) Airstream relative velocity V_A , flight-path angle γ_A , and azimuth σ_A .

Figure 5. - Continued.



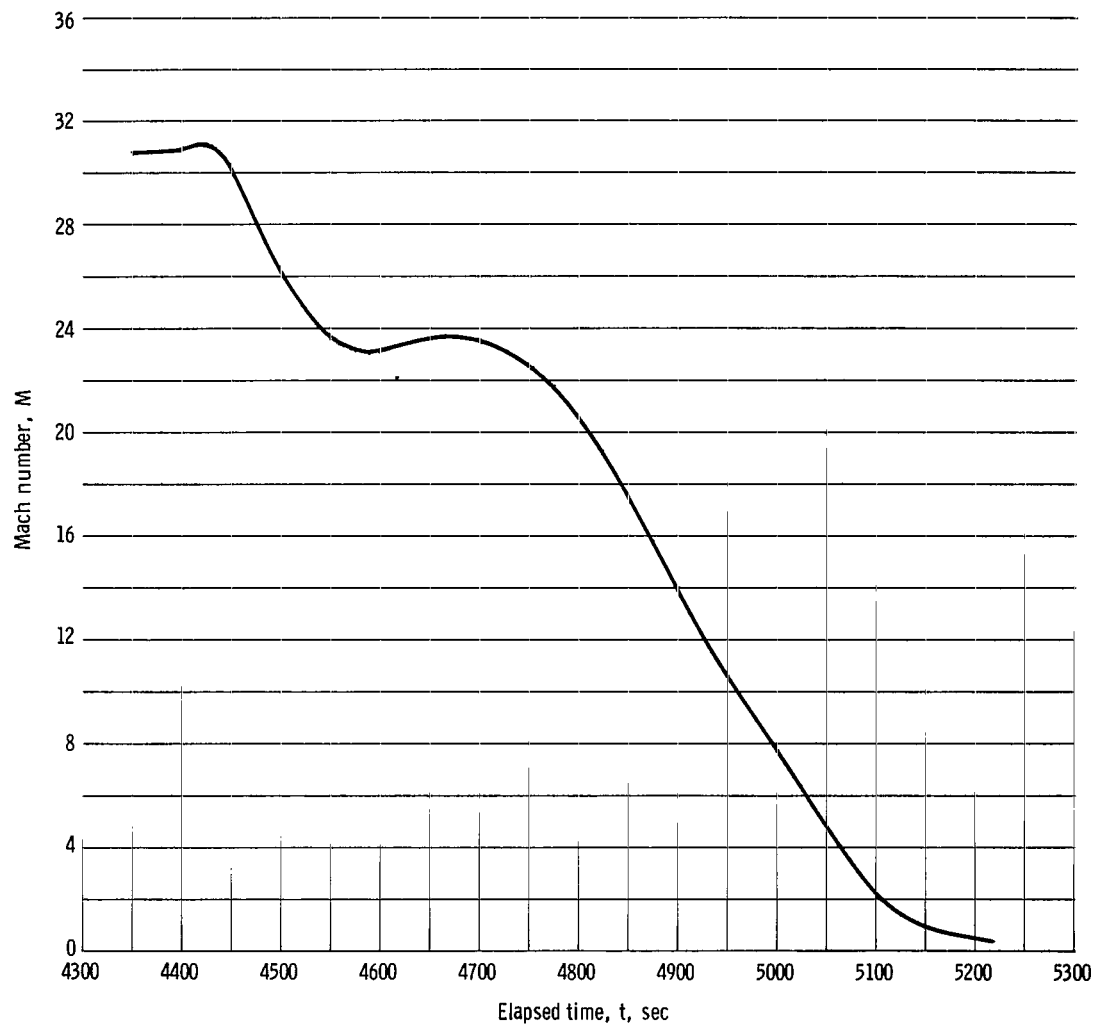
(c) Deceleration load factor L_f .

Figure 5. - Continued.



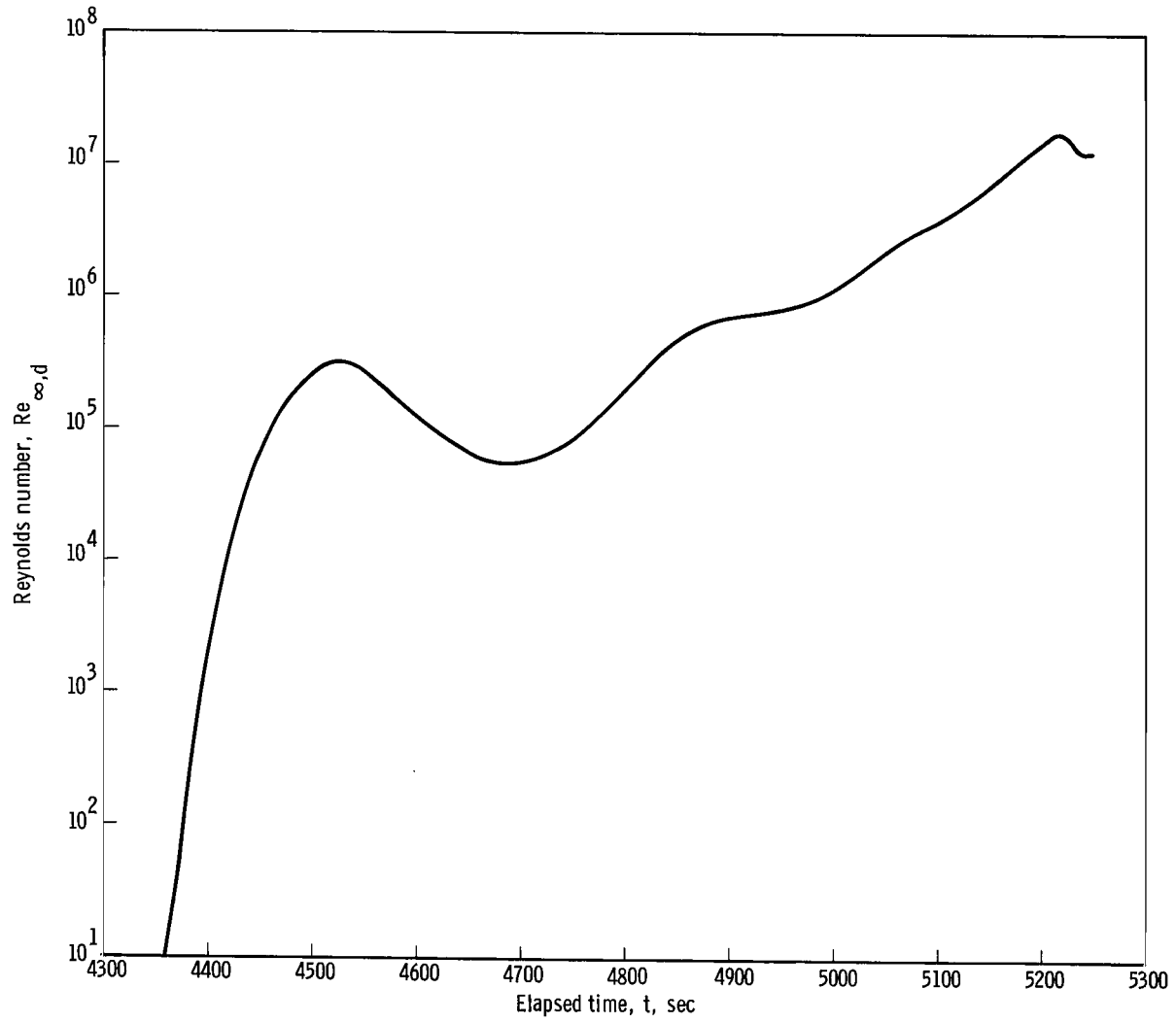
(d) Dynamic pressure q_{∞} .

Figure 5. - Continued.



(e) Mach number M.

Figure 5. - Continued.



(f) Reynolds number, $Re_{\infty, d}$ based on $d = 12.833$ feet.

Figure 5. - Concluded.

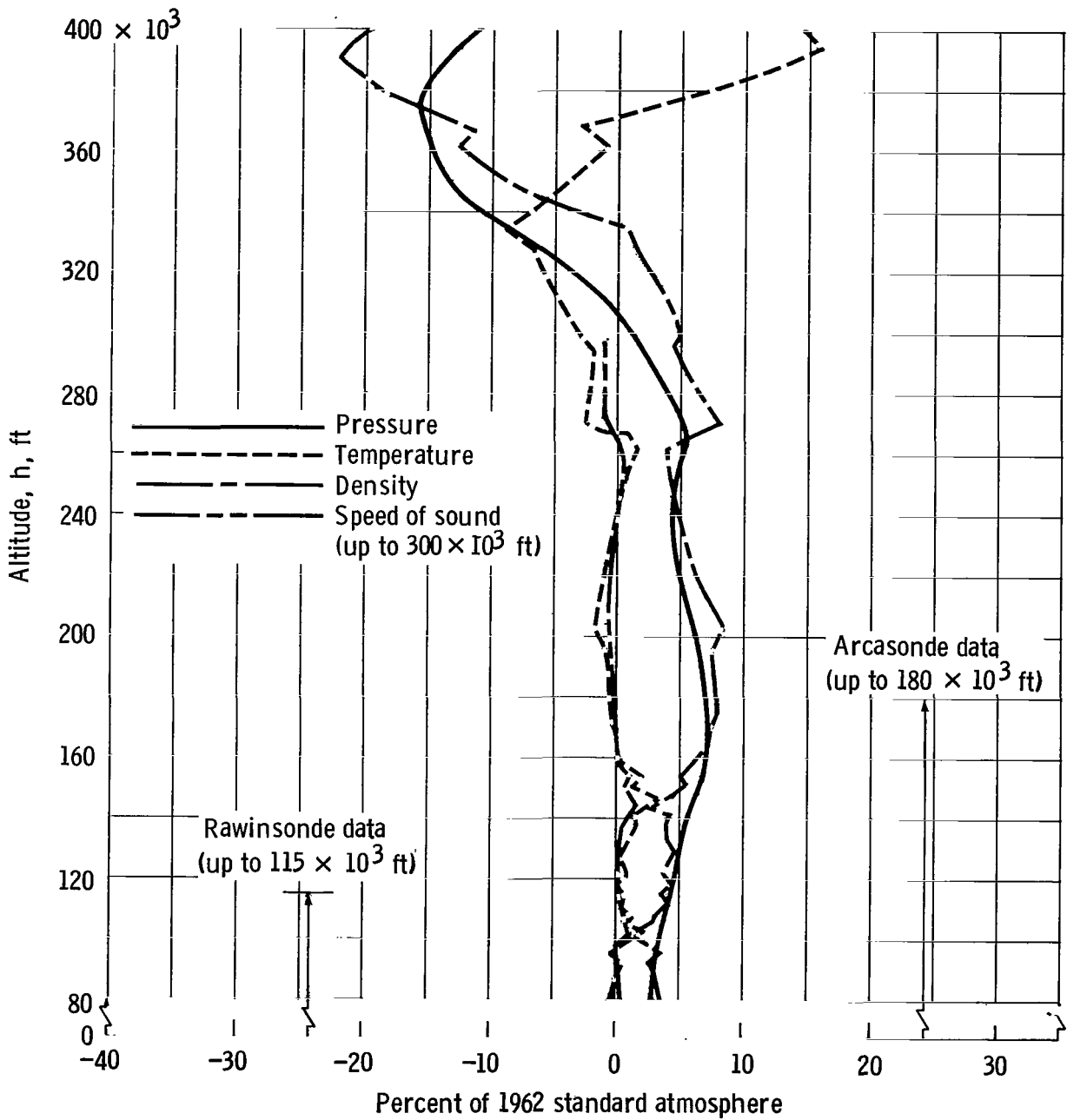
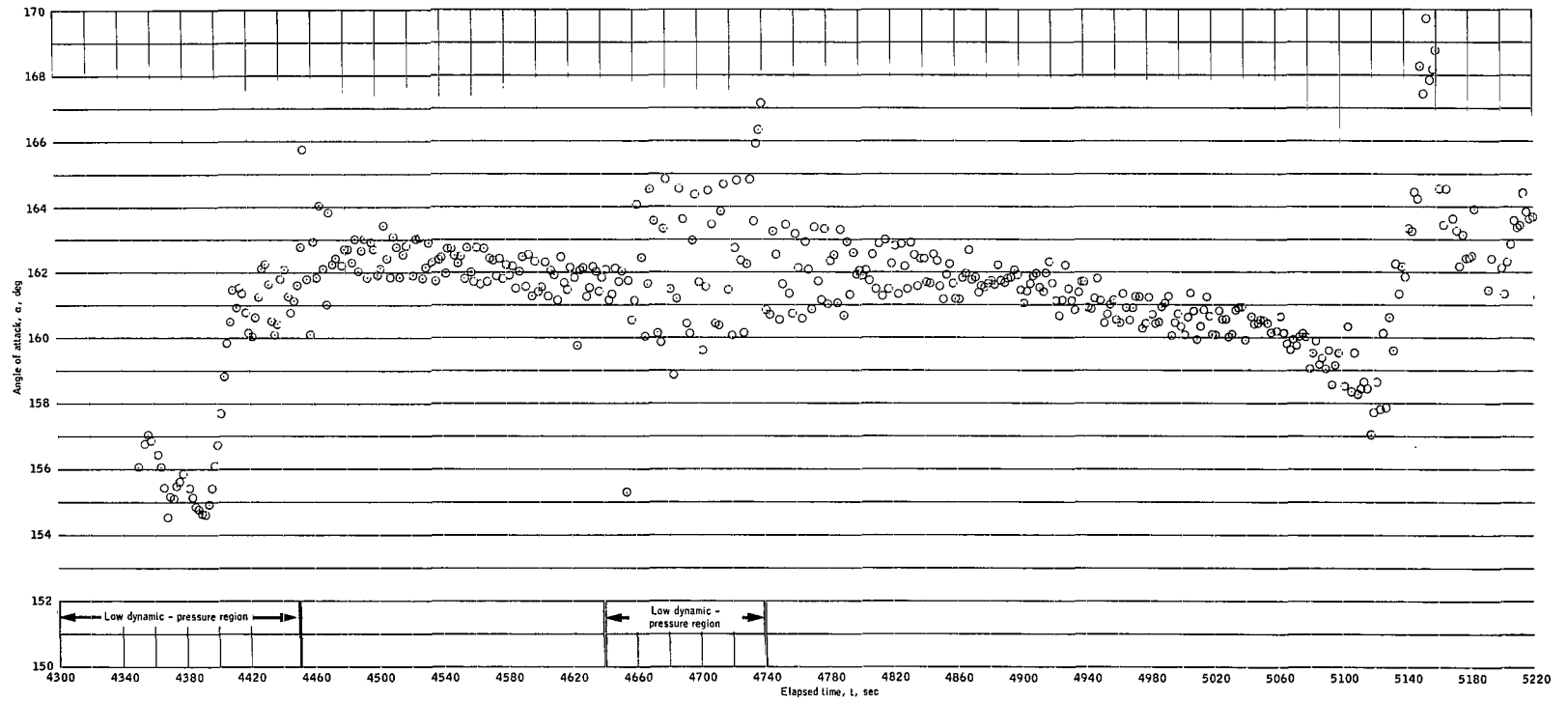
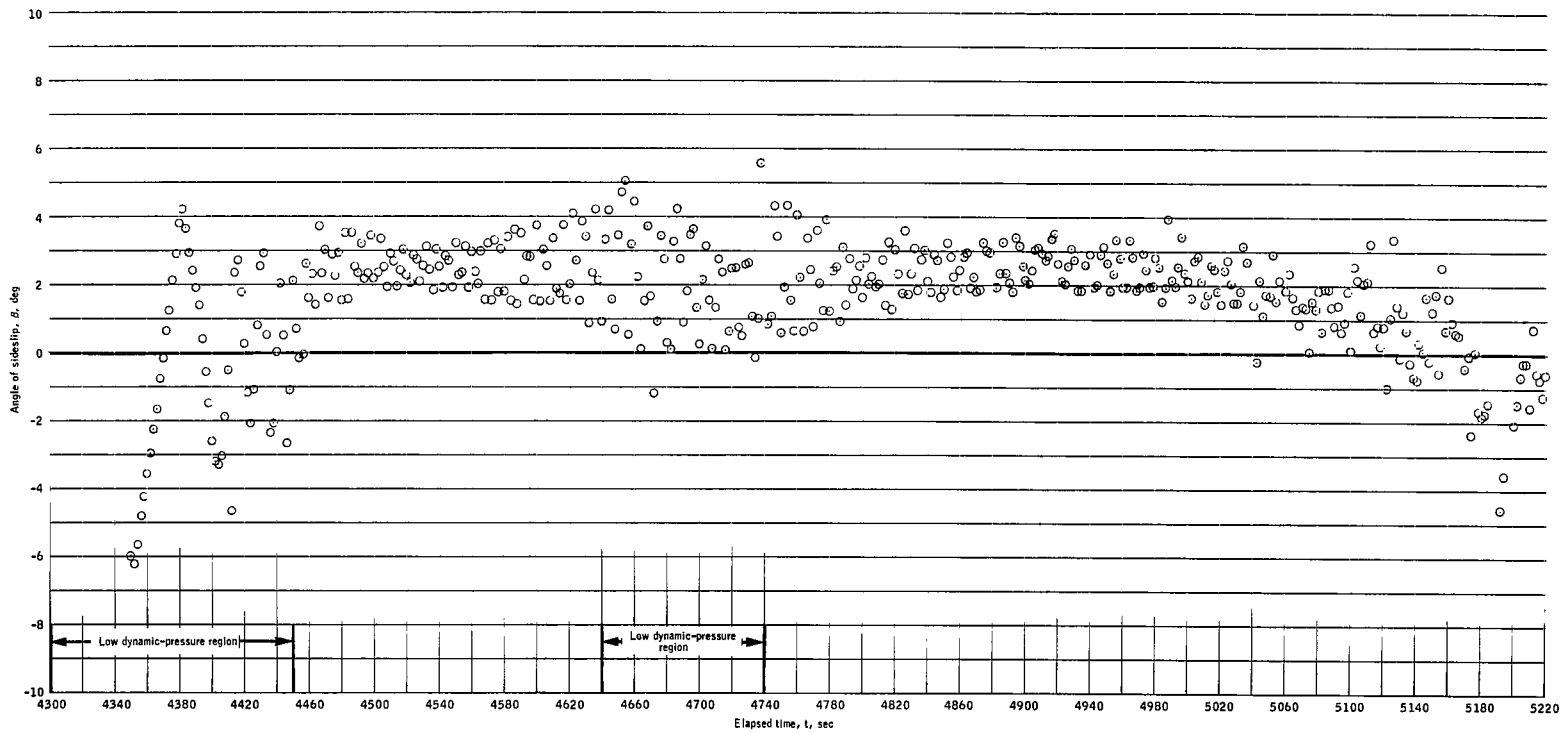


Figure 6. - Extrapolated postflight reentry atmospheric data, Mission AS-202.



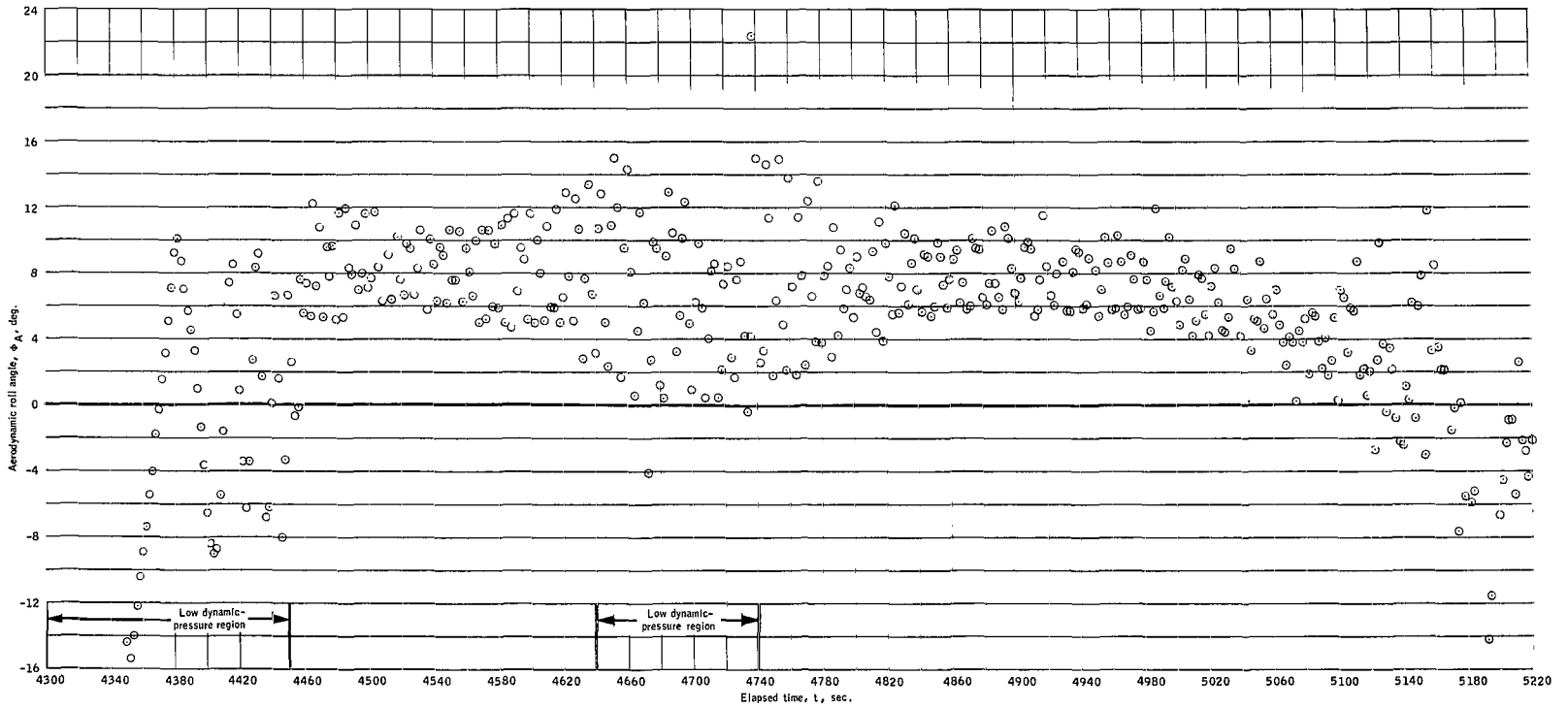
(a) Angle of attack α .

Figure 7. - Time histories of flight aerodynamic angles.



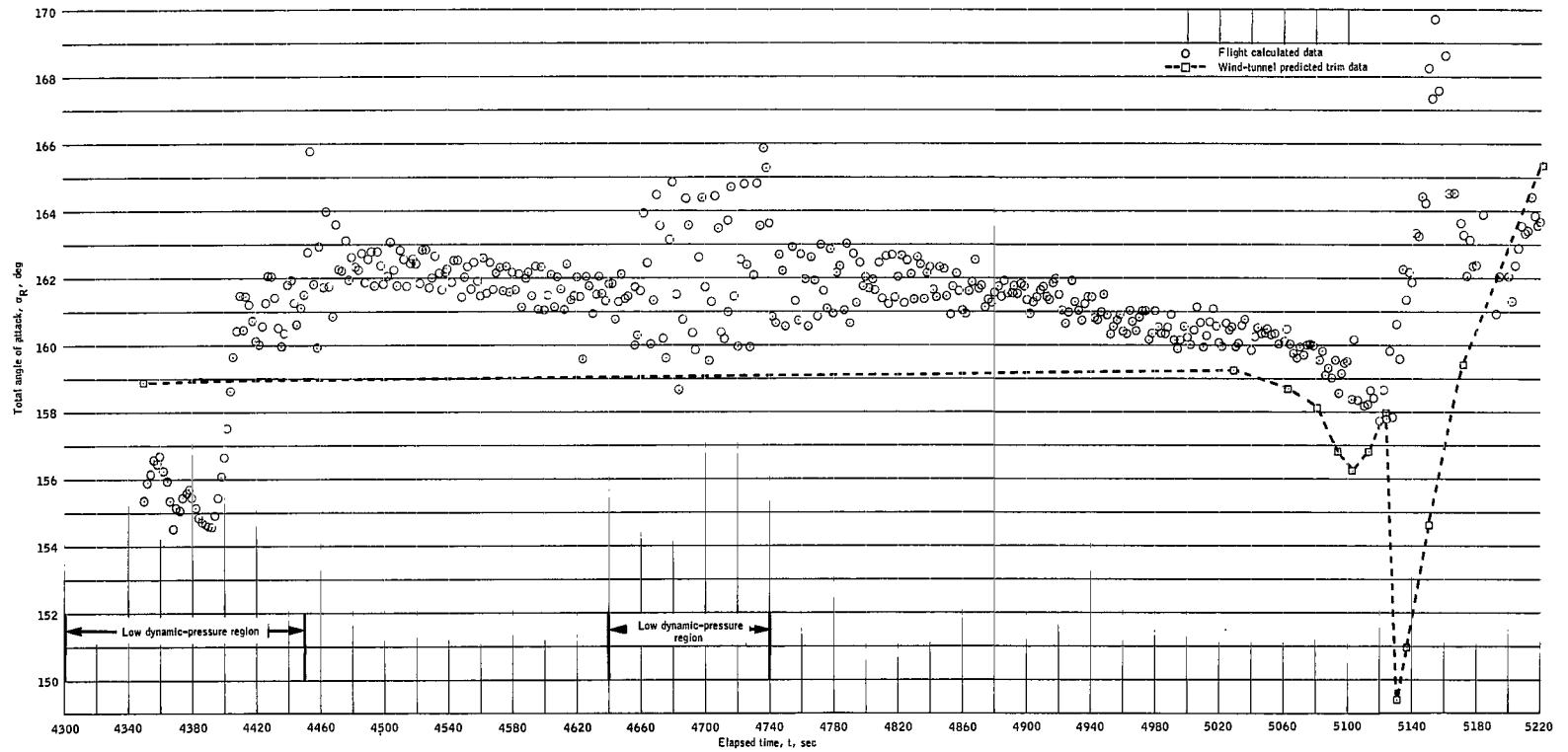
(b) Angle of sideslip β .

Figure 7. - Continued.



(c) Aerodynamic roll angle Φ_A .

Figure 7. - Continued.



(d) Total angle of attack α_R .

Figure 7. - Concluded.

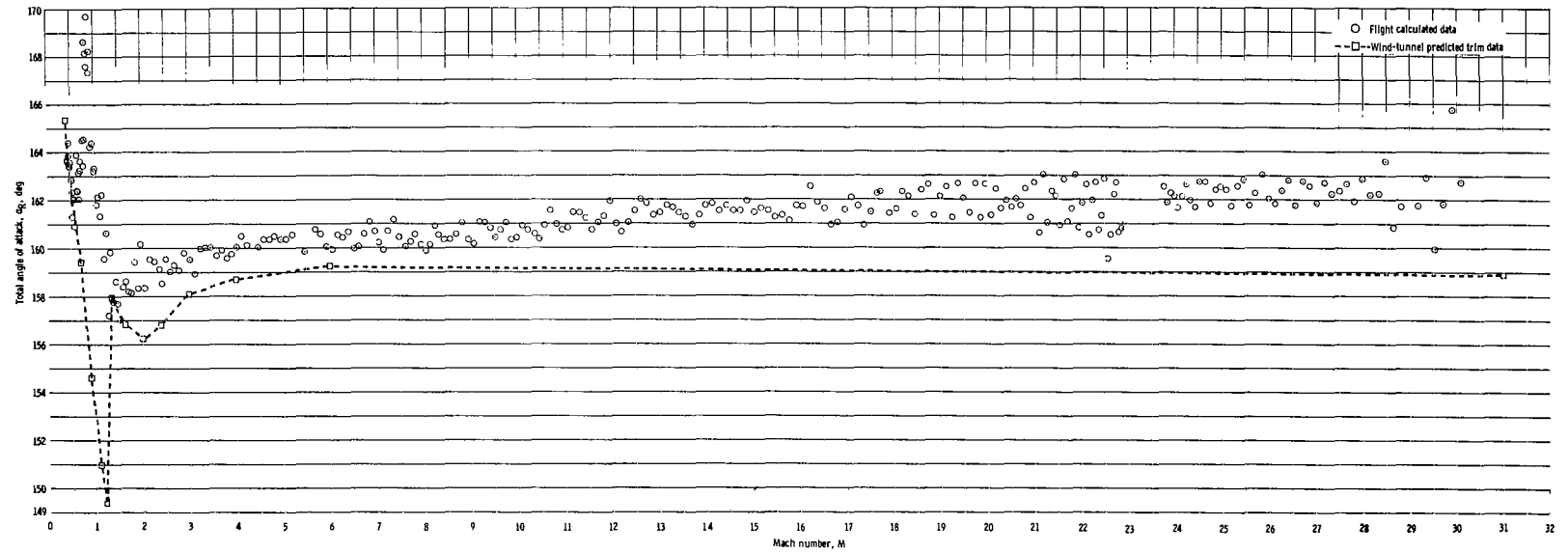
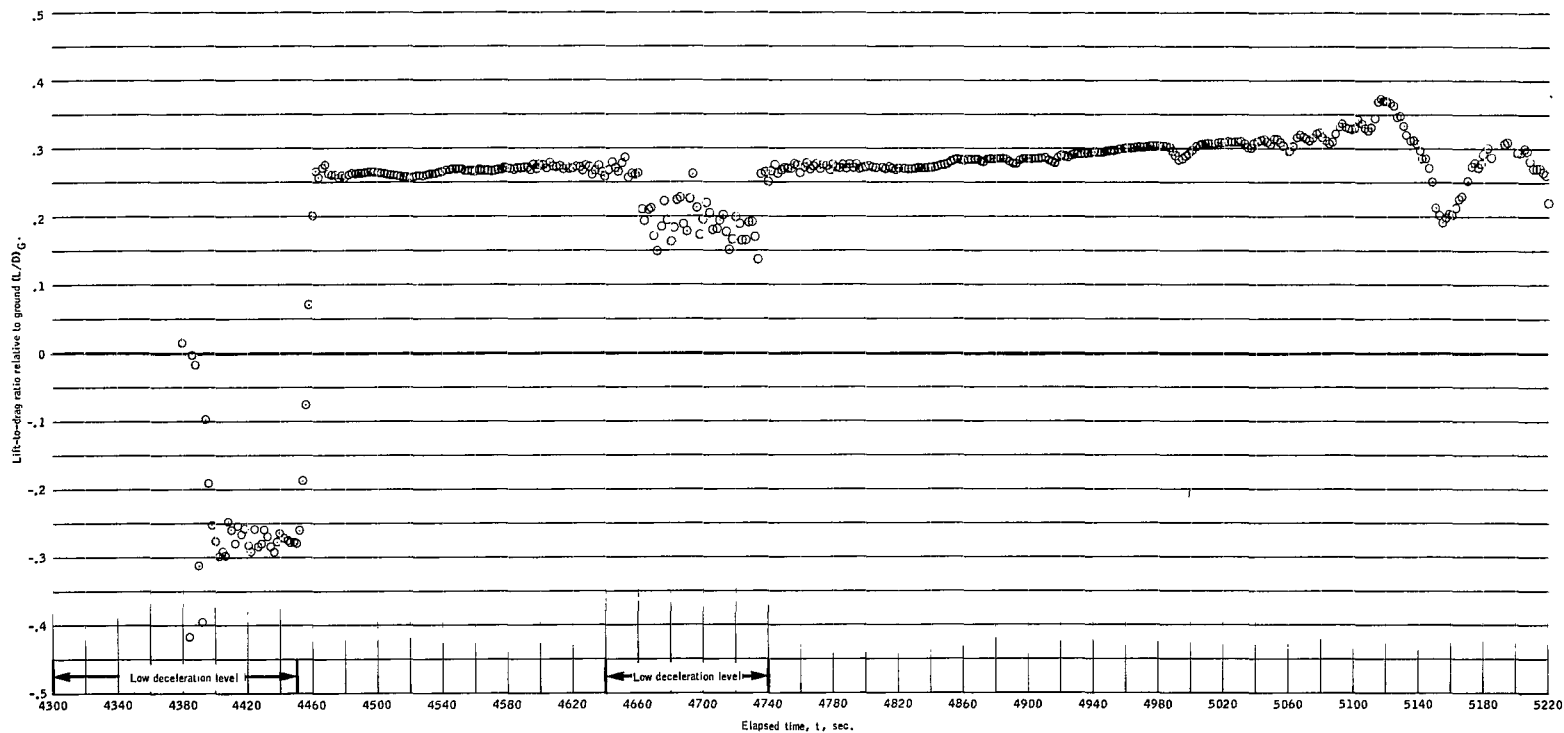
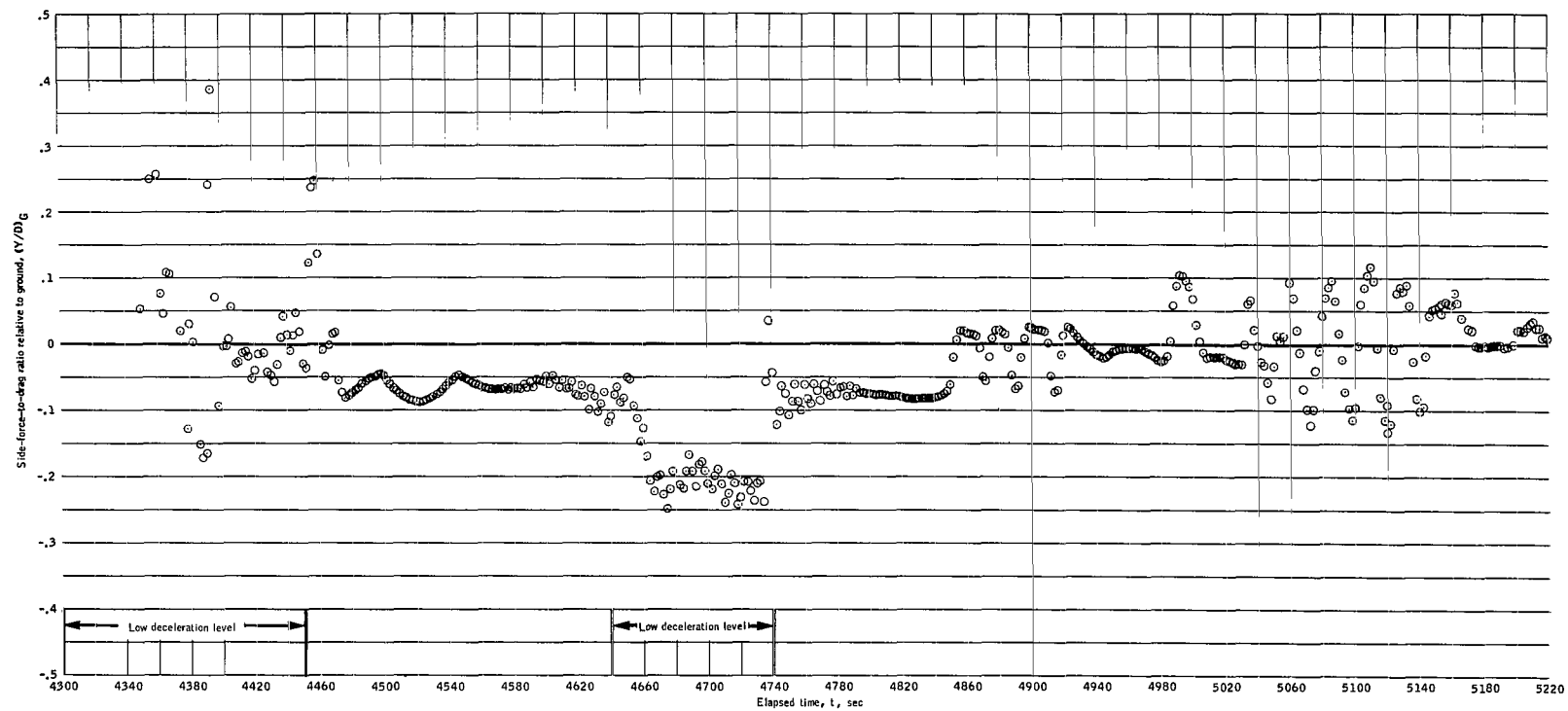


Figure 8. - Total flight angle of attack α_R plotted against Mach number M.
Data in the low dynamic-pressure region are omitted.



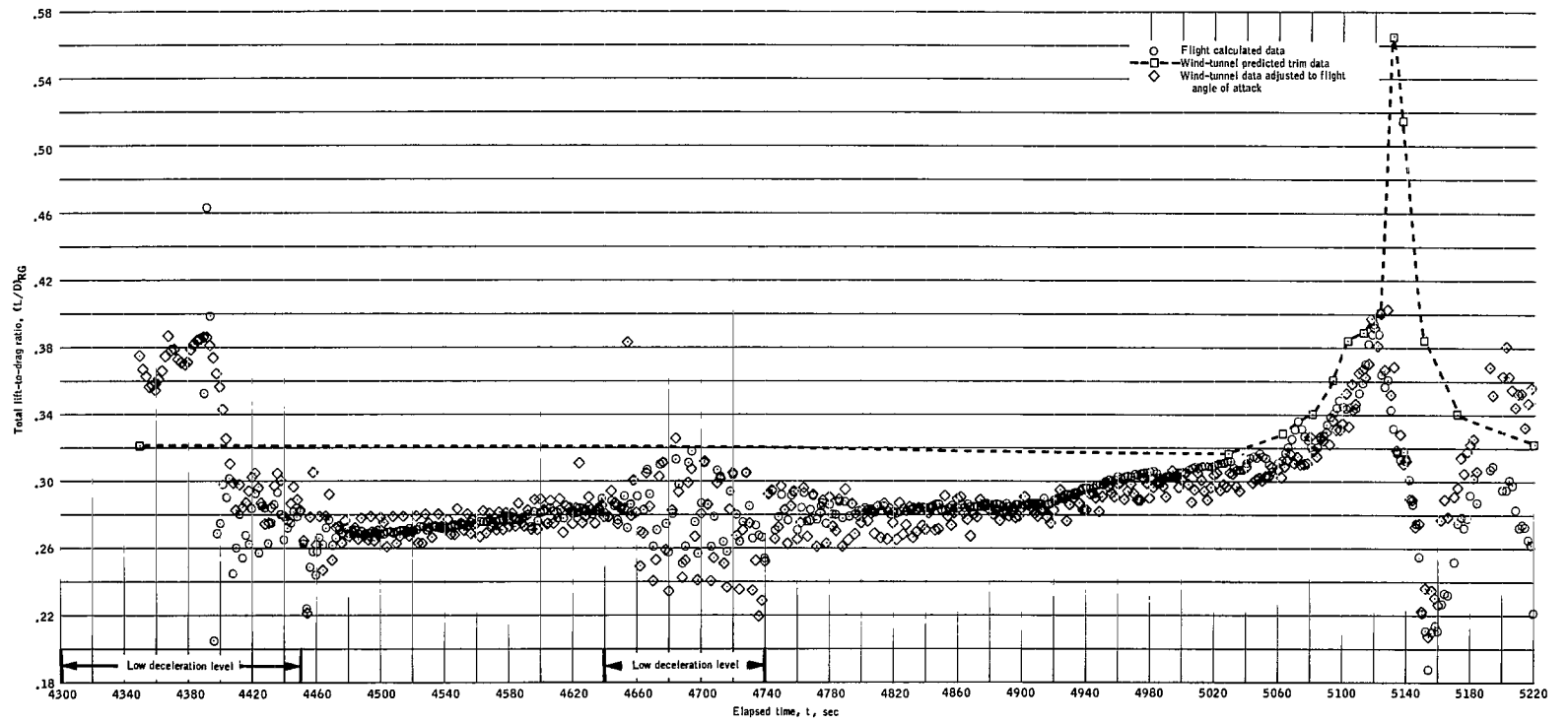
(a) Lift-to-drag ratio relative to ground $(L/D)_G$.

Figure 9. - Time histories of flight aerodynamic-coefficient ratios.



(b) Side-force-to-drag ratio relative to ground $(Y/D)_G$.

Figure 9. - Continued.



(c) Total lift-to-drag ratio $(L/D)_{RG}$.

Figure 9. - Concluded.

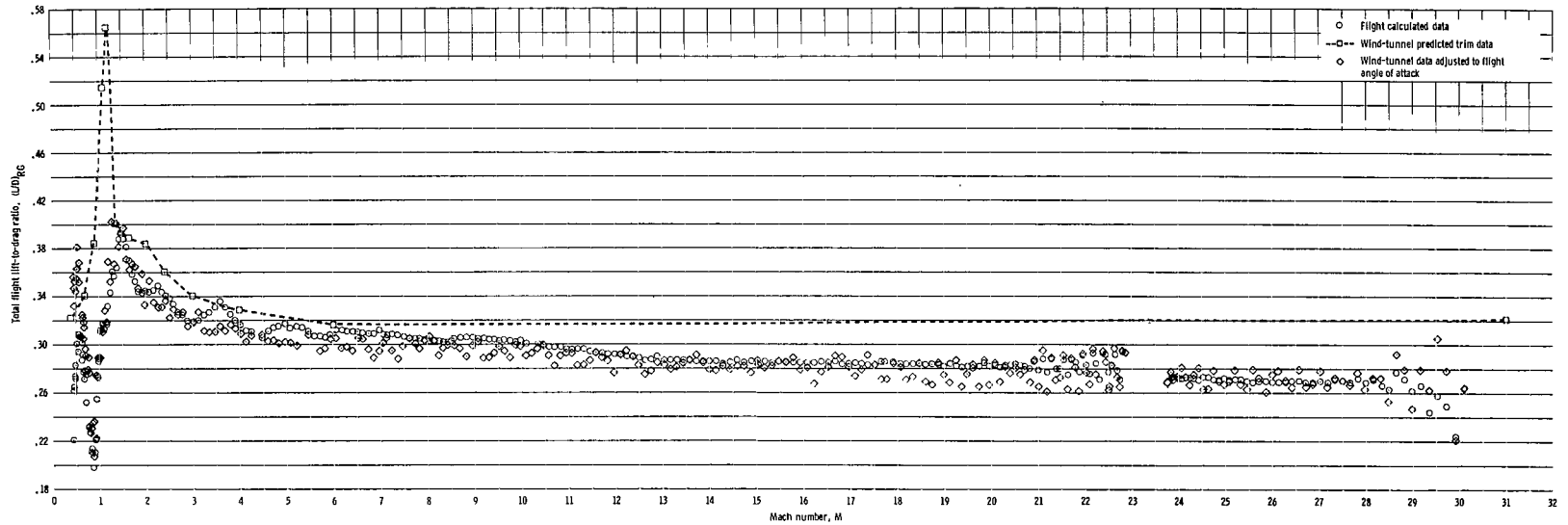
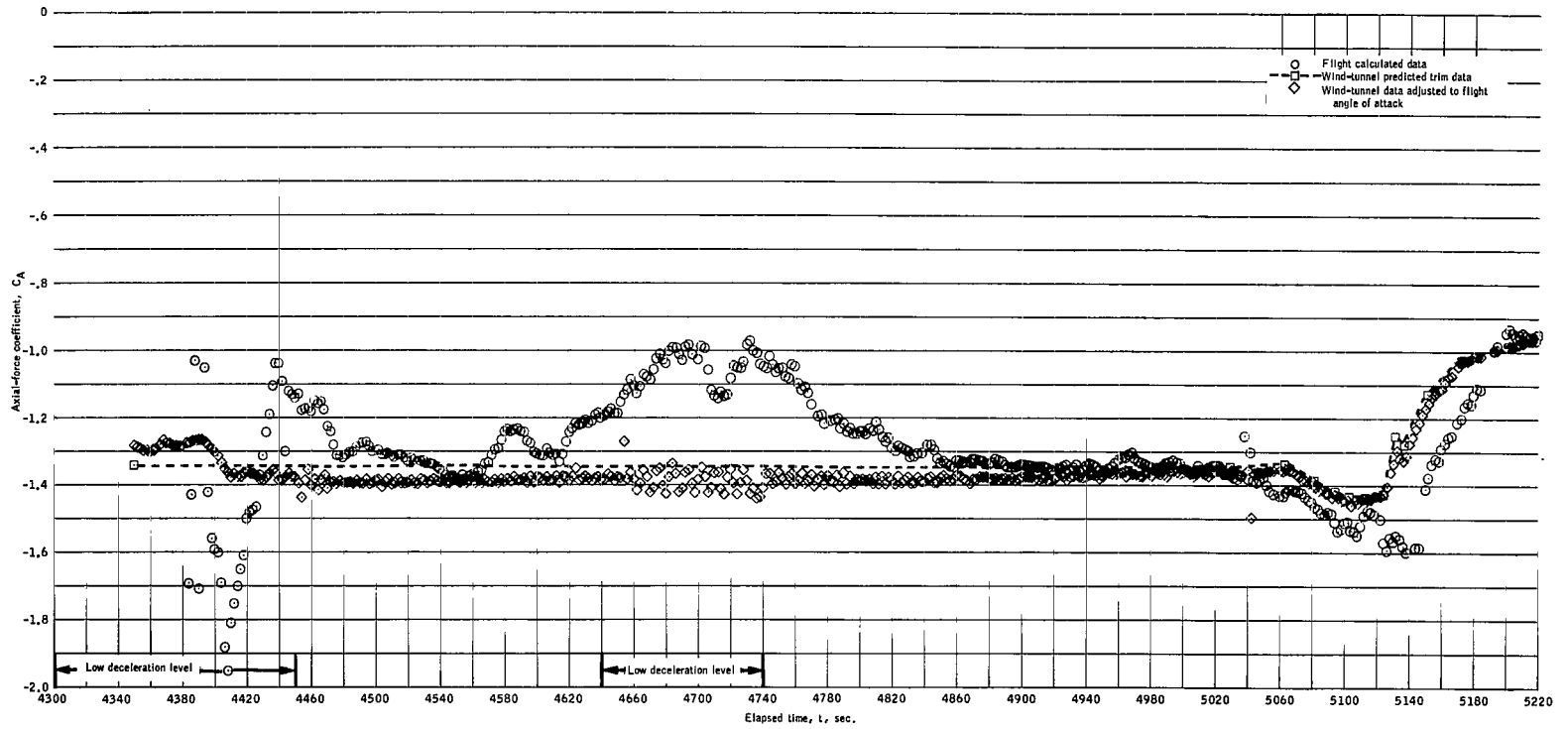
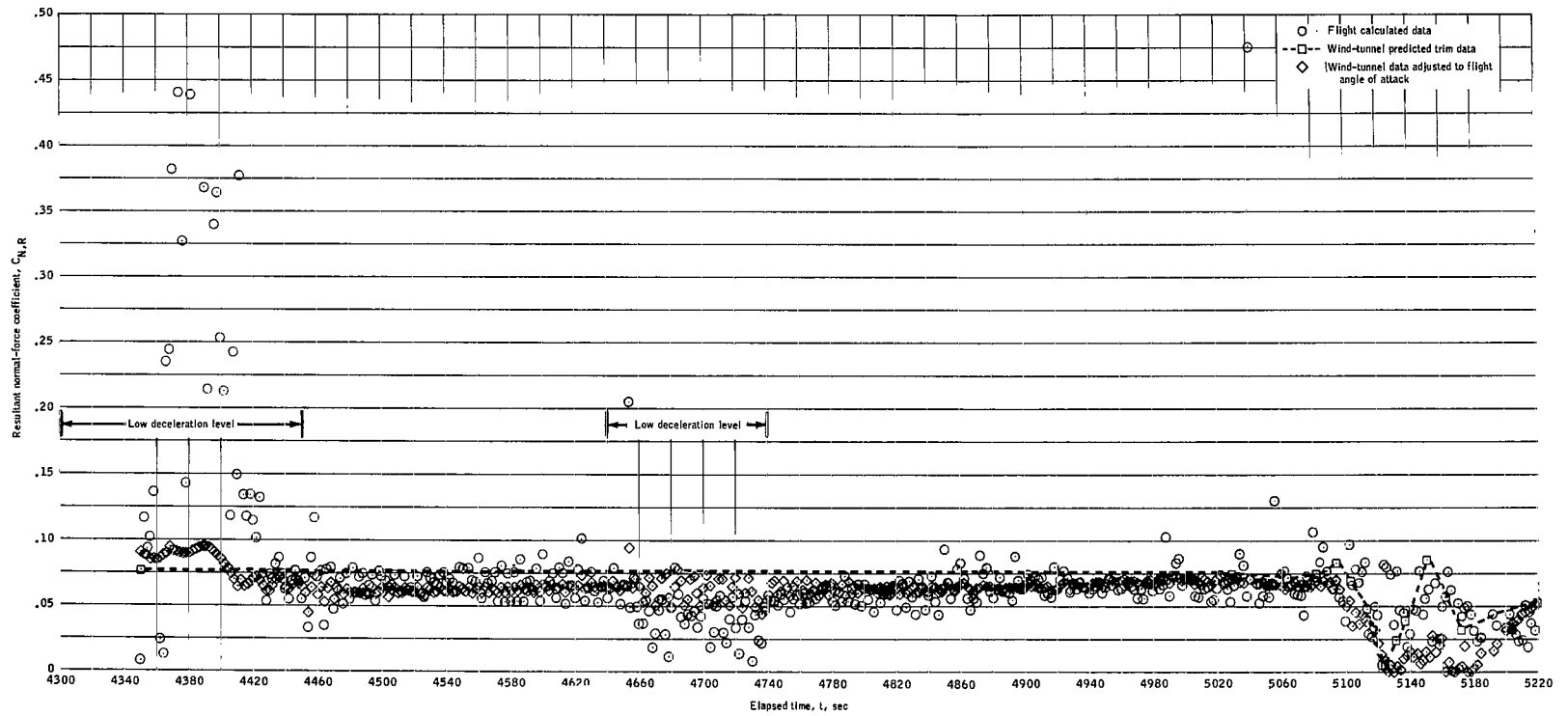


Figure 10. - Total flight lift-to-drag ratio $(L/D)_{RG}$ plotted against Mach number M .
Data in the low deceleration-level region are omitted.



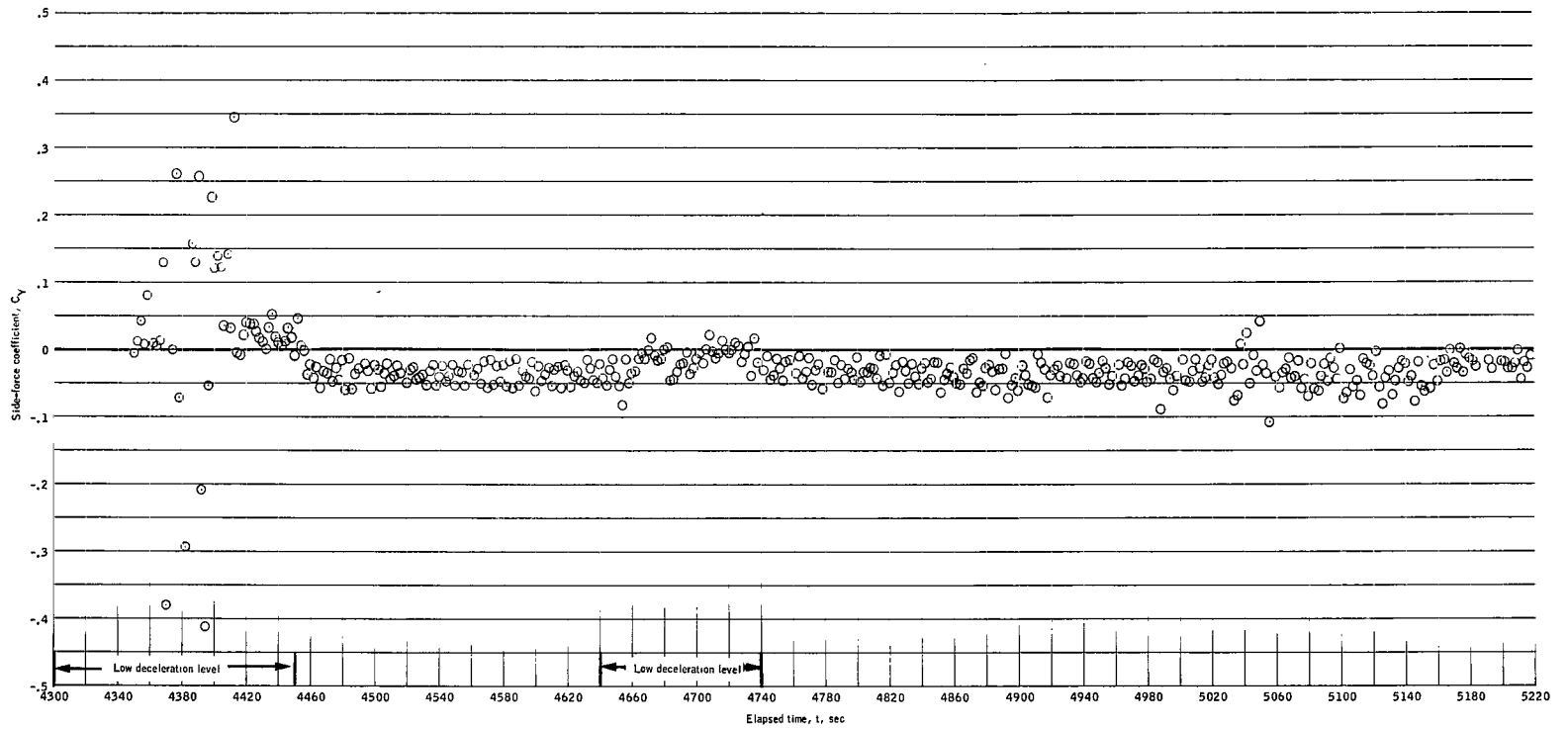
(a) Axial-force coefficient C_A .

Figure 11. - Time histories of flight body axis coefficients.



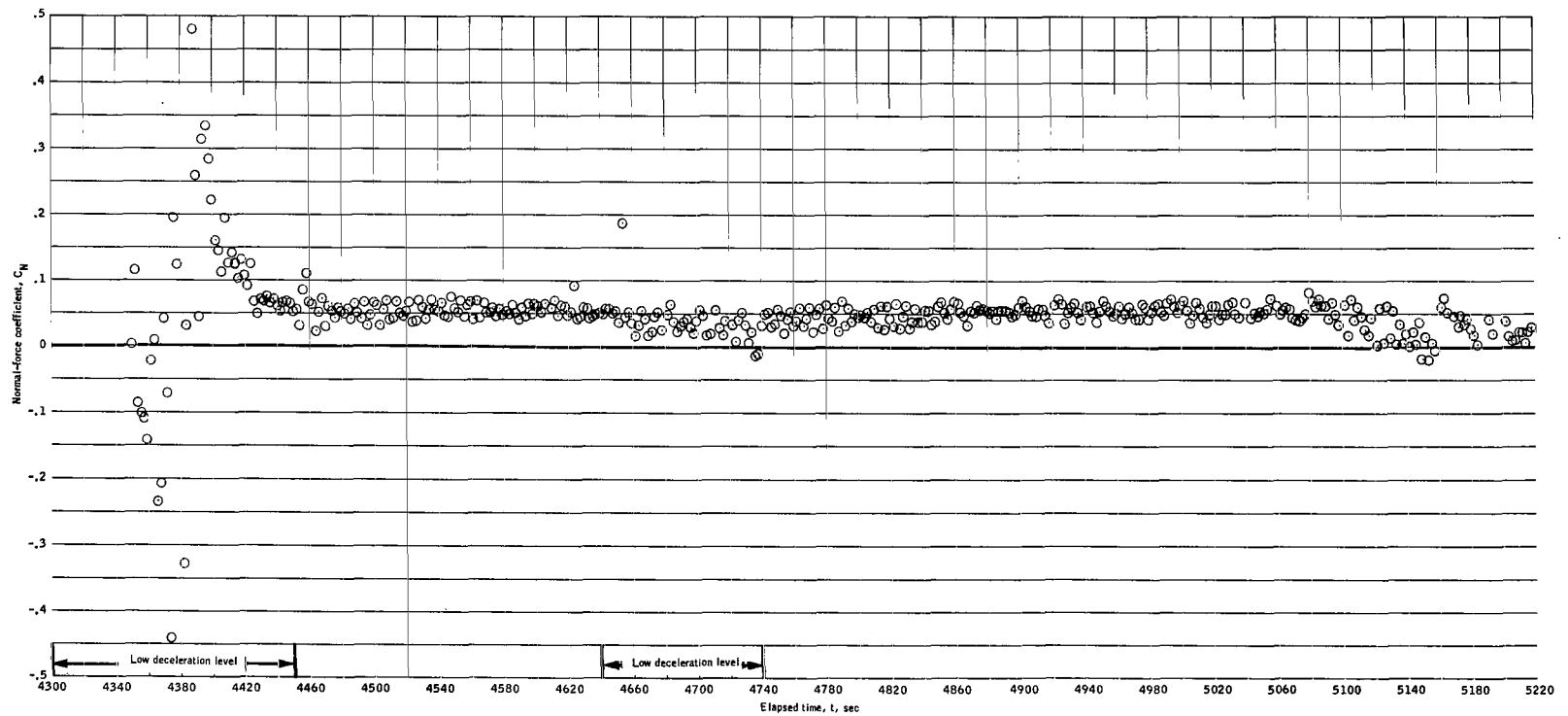
(b) Resultant normal-force coefficient $C_{N,R}$.

Figure 11. - Continued.



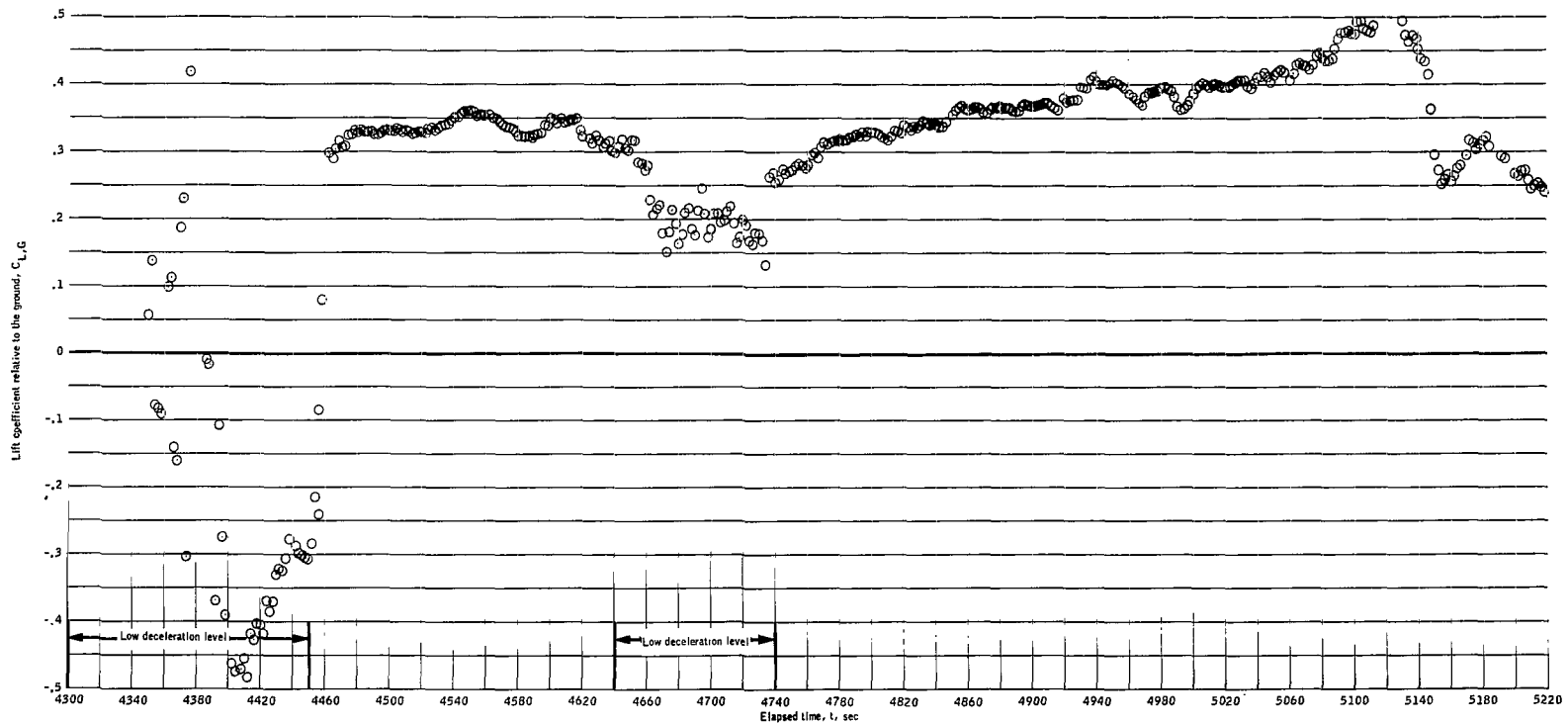
(c) Side-force coefficient C_Y .

Figure 11. - Continued.



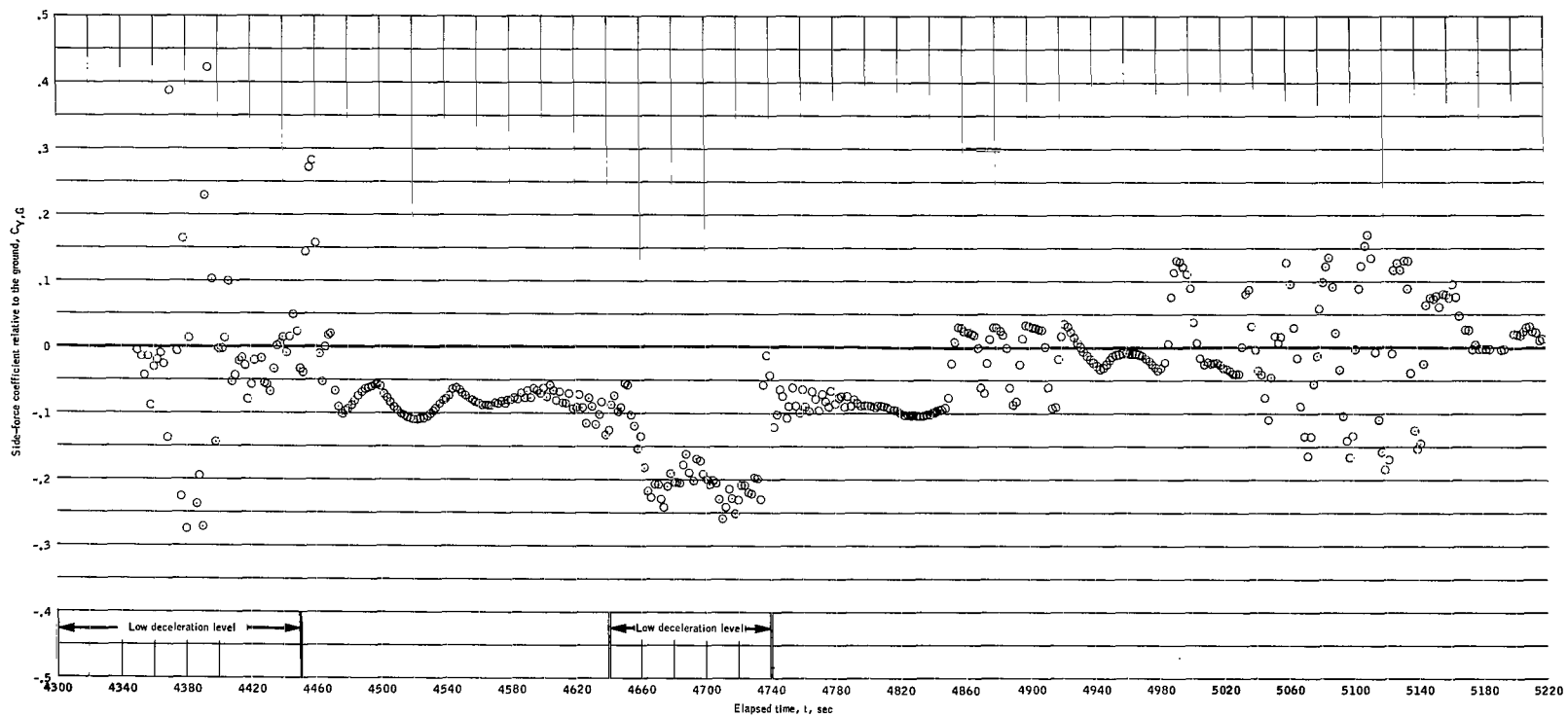
(d) Normal-force coefficient C_N .

Figure 11. - Concluded.



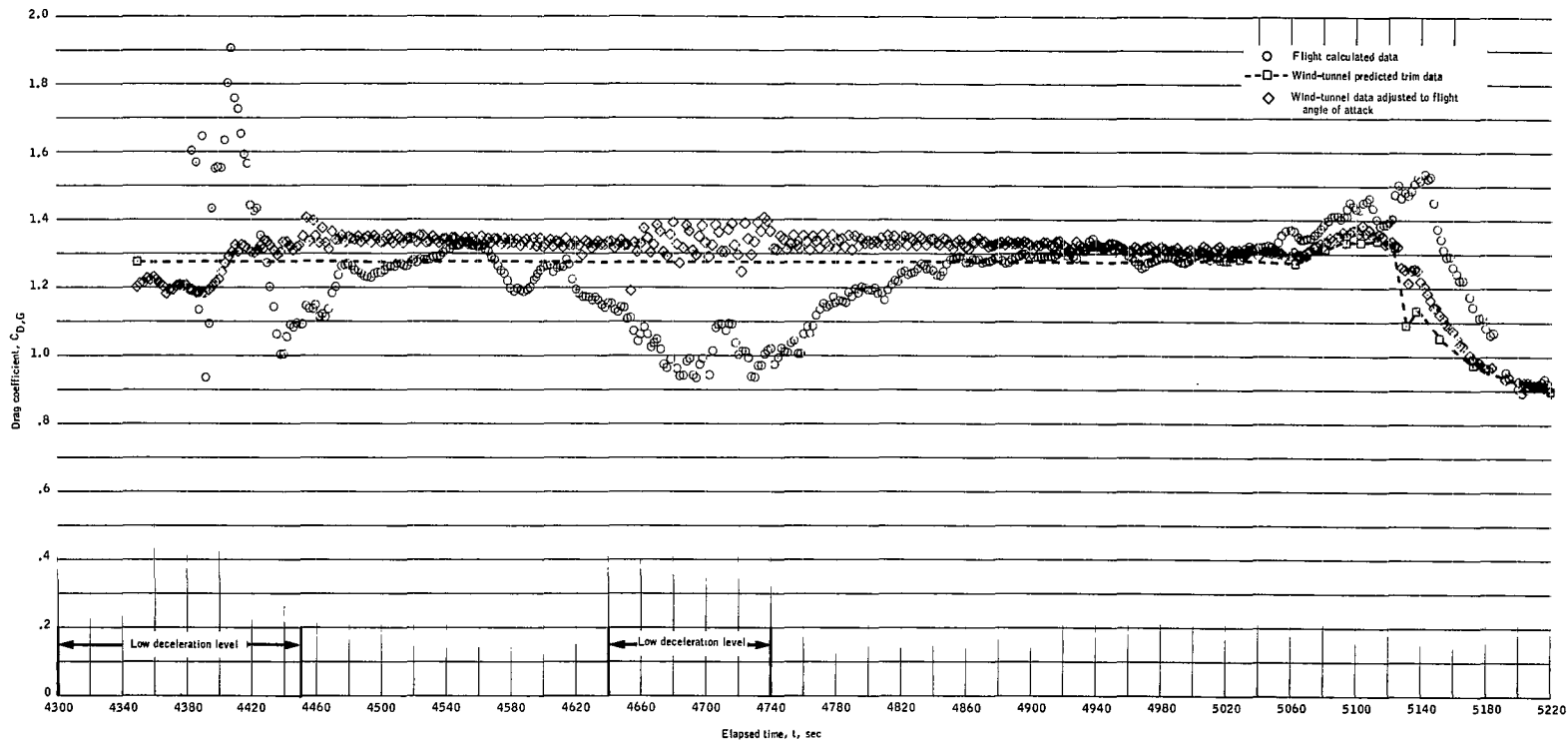
(a) Lift coefficient relative to the ground $C_{L,G}$.

Figure 12. - Time histories of flight force coefficients relative to the ground.



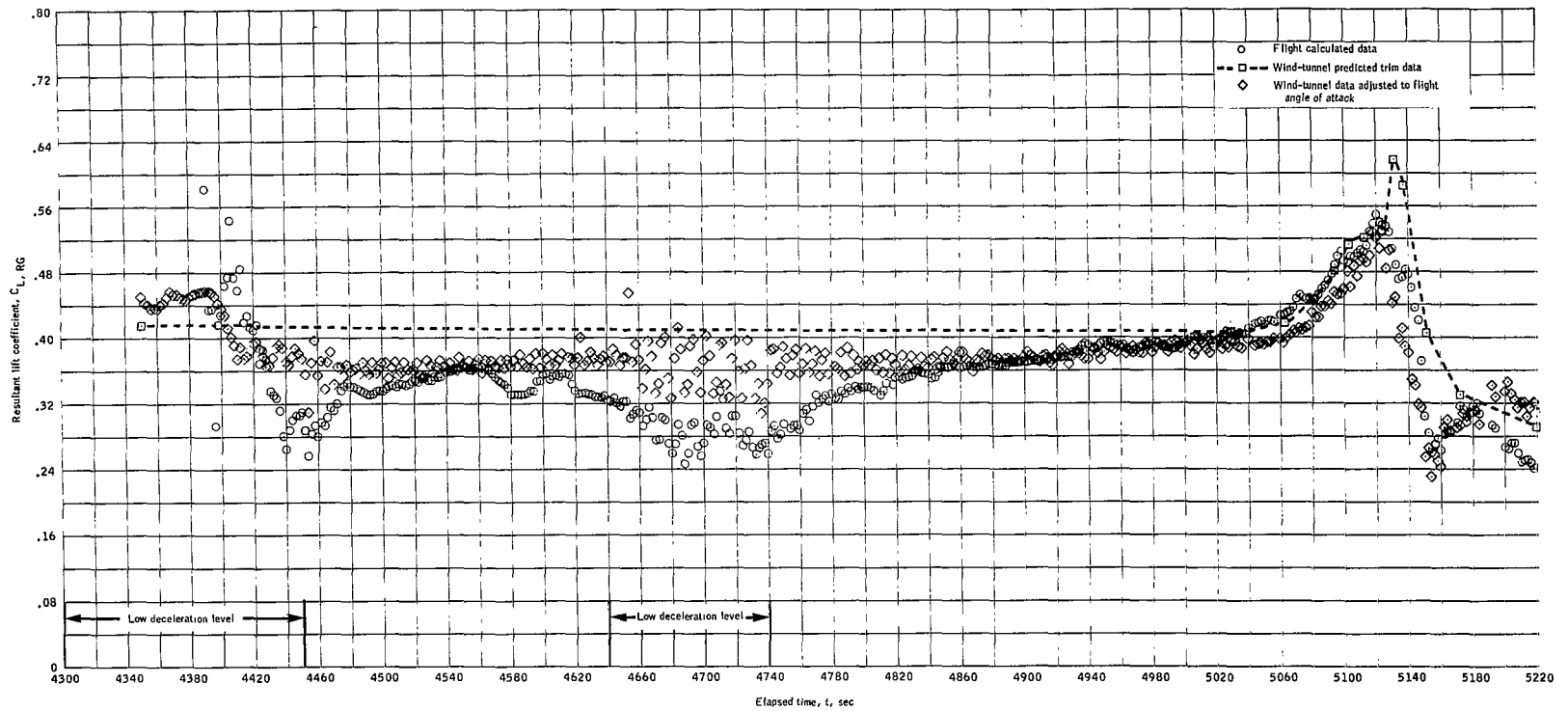
(b) Side-force coefficient relative to the ground $C_{Y, G}$

Figure 12. - Continued.



(c) Drag coefficient $C_{D,G}$.

Figure 12, - Continued.



(d) Resultant lift coefficient $C_{L, RG}$.

Figure 12. - Concluded.

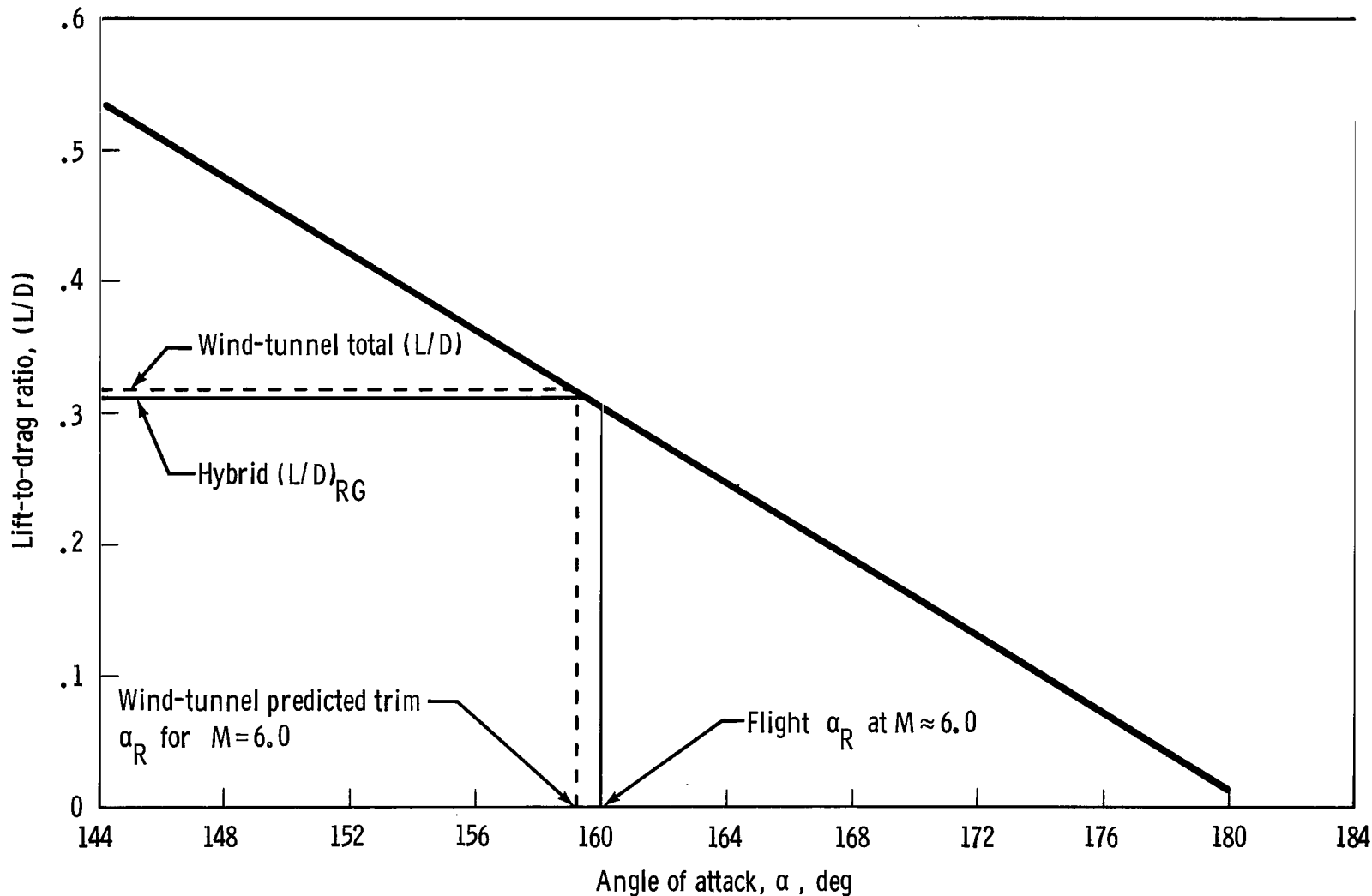
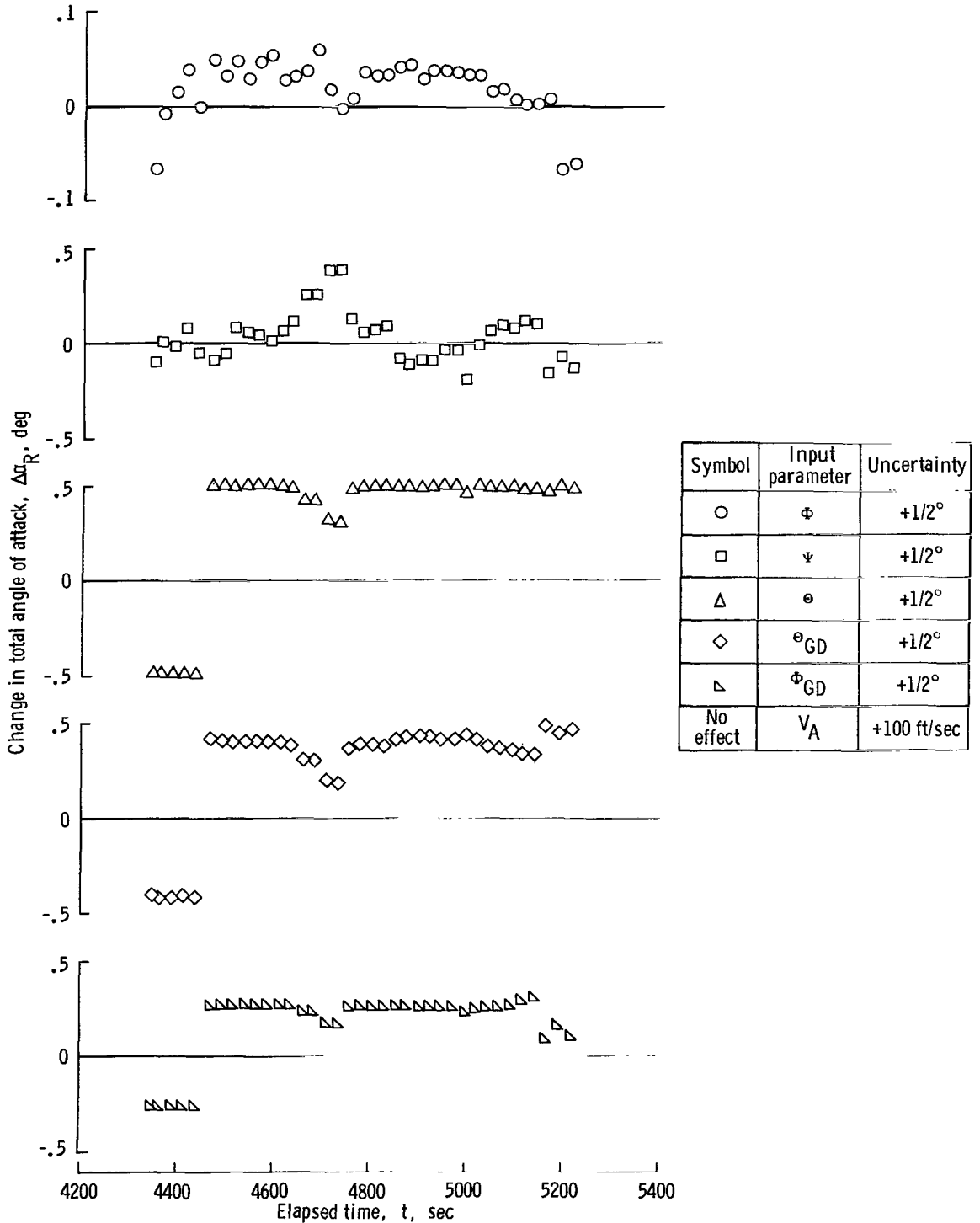
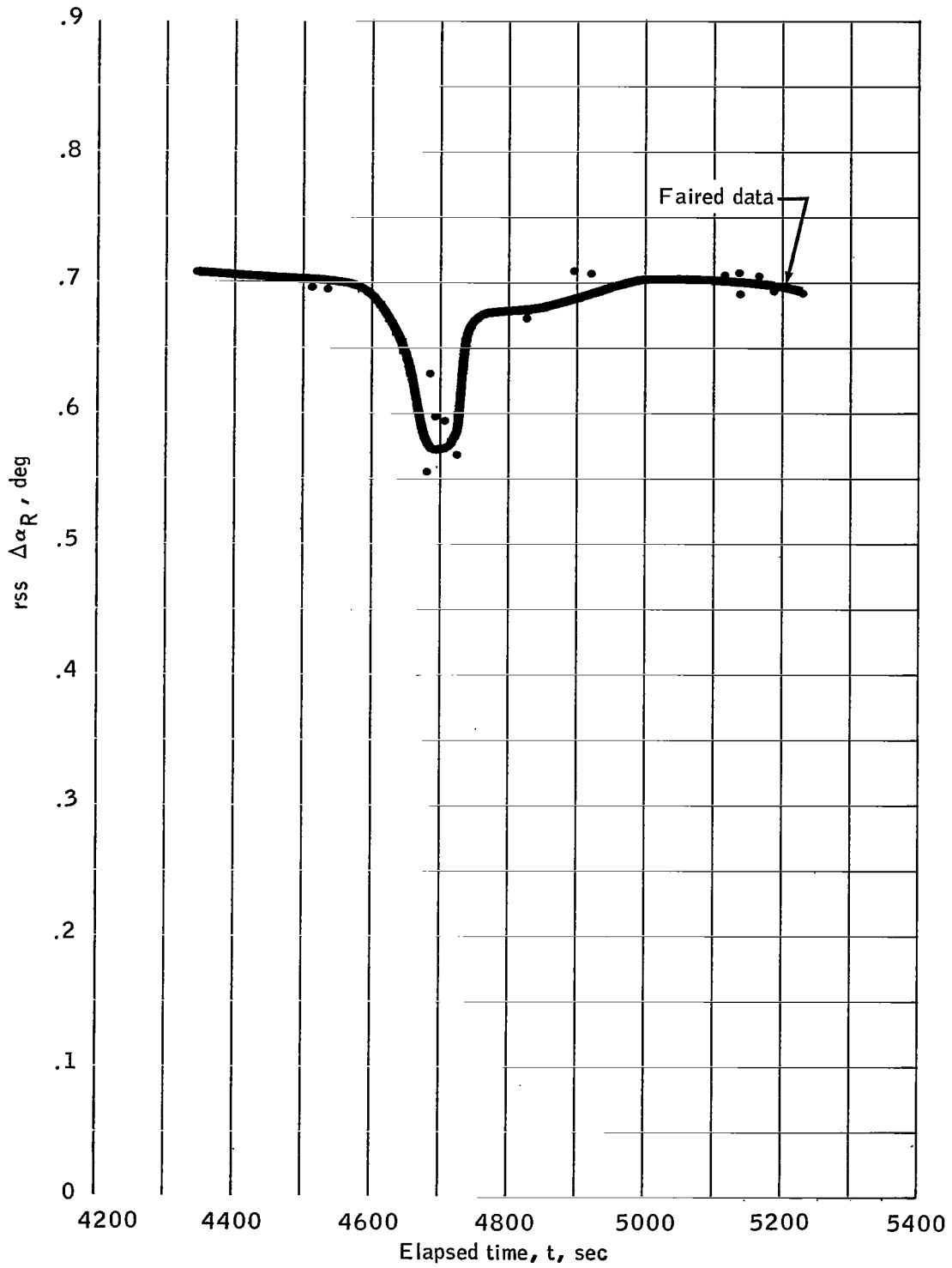


Figure 13. - Example of the source of the wind-tunnel data adjusted to flight angle of attack or the hybrid data method. Shown are wind-tunnel data for lift-to-drag ratio L/D plotted against angle of attack α for $M = 6.0$.



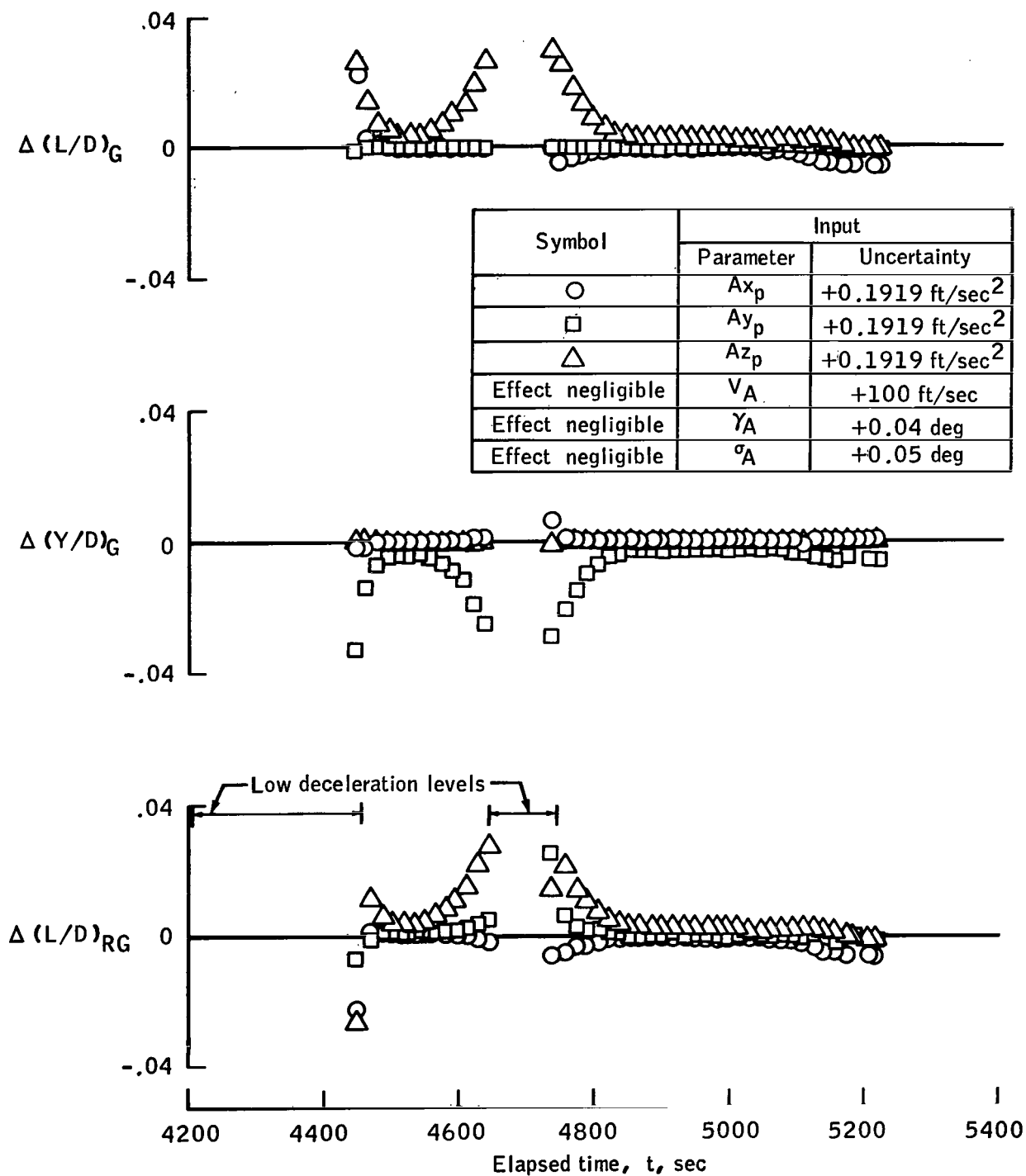
(a) Total angle-of-attack α_R delta values.

Figure 14. - Effects of flight-data uncertainties on the calculated aerodynamic data.



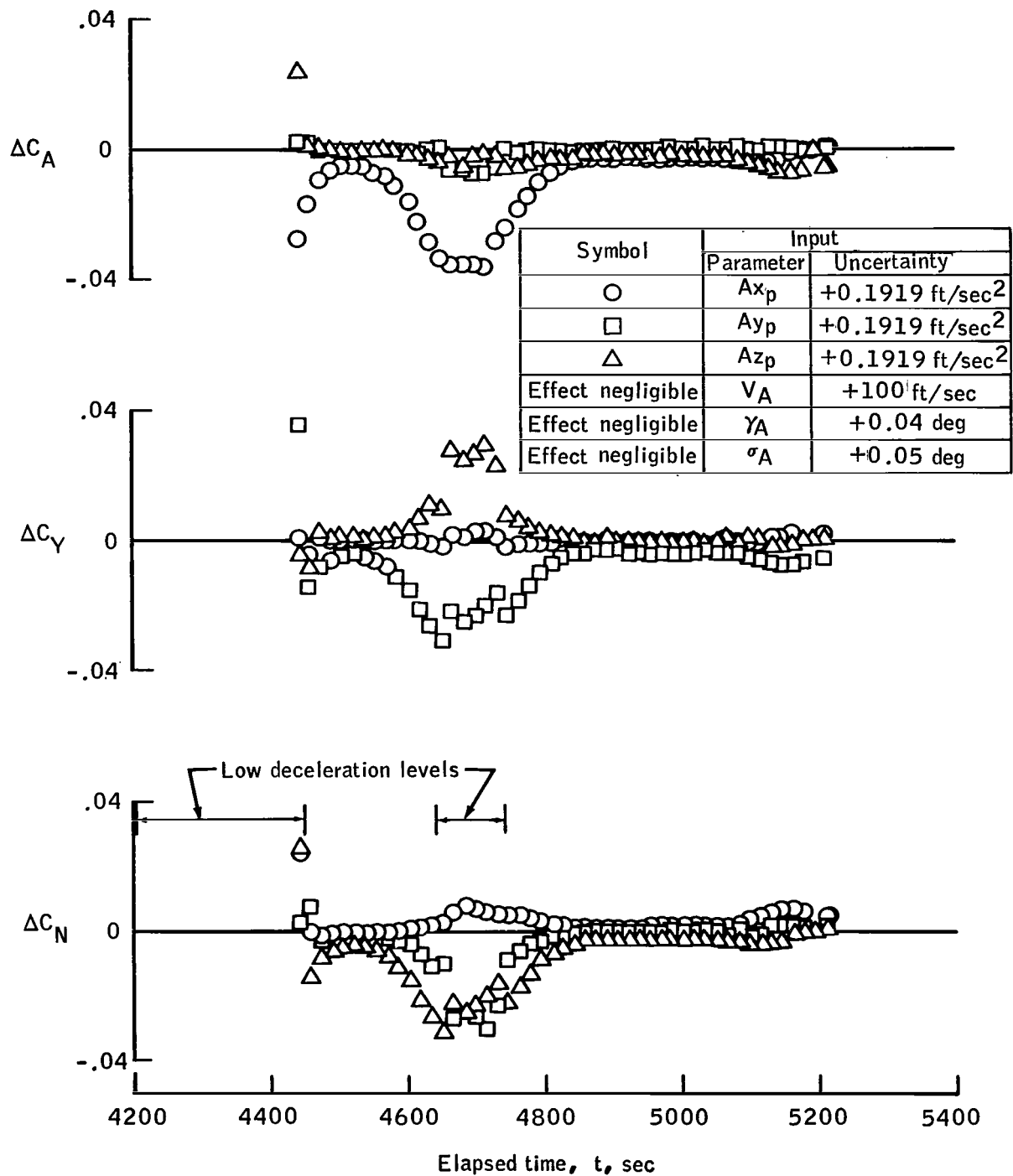
(b) Total angle-of-attack α_R rss delta values.

Figure 14. - Continued.



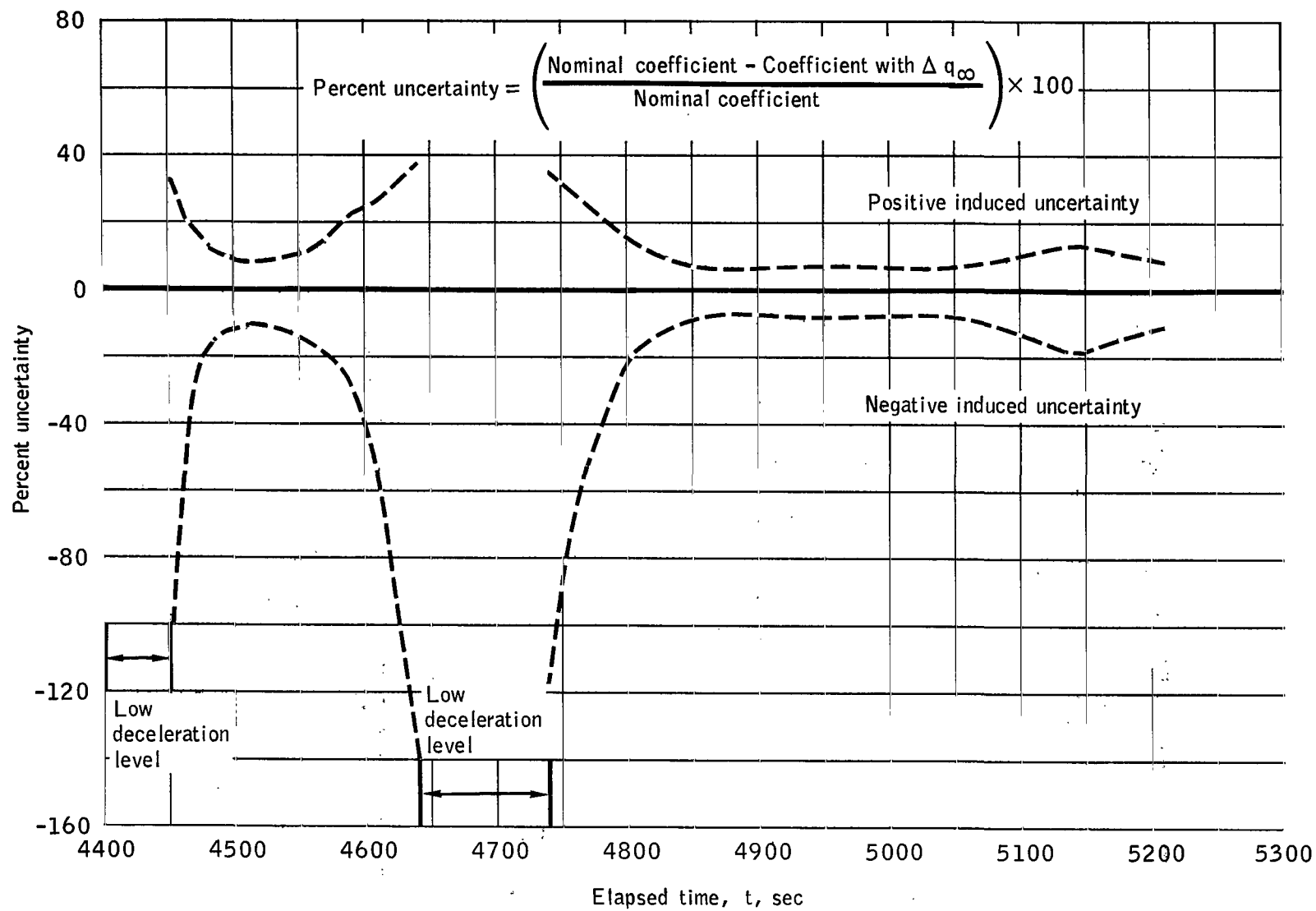
(c) Coefficient-ratio delta values.

Figure 14. - Continued.



(d) Body axis coefficient delta values.

Figure 14. - Continued.



(e) Percent uncertainty in all flight coefficient data caused by an uncertainty of measured stagnation pressure of 3 percent of full-scale reading.

Figure 14. - Concluded.

"The aeronautical and space activities of the United States shall be conducted so as to contribute . . . to the expansion of human knowledge of phenomena in the atmosphere and space. The Administration shall provide for the widest practicable and appropriate dissemination of information concerning its activities and the results thereof."

—NATIONAL AERONAUTICS AND SPACE ACT OF 1958

NASA SCIENTIFIC AND TECHNICAL PUBLICATIONS

TECHNICAL REPORTS: Scientific and technical information considered important, complete, and a lasting contribution to existing knowledge.

TECHNICAL NOTES: Information less broad in scope but nevertheless of importance as a contribution to existing knowledge.

TECHNICAL MEMORANDUMS: Information receiving limited distribution because of preliminary data, security classification, or other reasons.

CONTRACTOR REPORTS: Scientific and technical information generated under a NASA contract or grant and considered an important contribution to existing knowledge.

TECHNICAL TRANSLATIONS: Information published in a foreign language considered to merit NASA distribution in English.

SPECIAL PUBLICATIONS: Information derived from or of value to NASA activities. Publications include conference proceedings, monographs, data compilations, handbooks, sourcebooks, and special bibliographies.

TECHNOLOGY UTILIZATION PUBLICATIONS: Information on technology used by NASA that may be of particular interest in commercial and other non-aerospace applications. Publications include Tech Briefs, Technology Utilization Reports and Notes, and Technology Surveys.

Details on the availability of these publications may be obtained from:

SCIENTIFIC AND TECHNICAL INFORMATION DIVISION
NATIONAL AERONAUTICS AND SPACE ADMINISTRATION
Washington, D.C. 20546